



Cite this: *Catal. Sci. Technol.*, 2023, **13**, 4701

## A computational study of CO<sub>2</sub> hydrogenation on single atoms of Pt, Pd, Ni and Rh on In<sub>2</sub>O<sub>3</sub>(111)†

Francesco Cannizzaro, Sjoerd Kurstjens, Tom van den Berg,  
Emiel J. M. Hensen \* and Ivo A. W. Filot \*

Metal promoted indium oxide (In<sub>2</sub>O<sub>3</sub>) catalysts are promising materials for CO<sub>2</sub> hydrogenation to products such as methanol and carbon monoxide. The influence of the dispersion of the promoting metal on the methanol selectivity of In<sub>2</sub>O<sub>3</sub> catalysts is a matter of debate, which centers around the role of atomically dispersed single metal atoms vs. metal clusters as catalysts for methanol formation. In this study, we used density functional theory calculations to compare the role of single atoms (SAs) of Ni, Pd, Pt and Rh placed on the In<sub>2</sub>O<sub>3</sub>(111) surface to study CO<sub>2</sub> hydrogenation to CO and methanol. Direct and hydrogen-assisted CO<sub>2</sub> dissociation pathways leading to CO as well as methanol formation *via* either formate or CO intermediates are explicitly considered. Microkinetic simulations show that all SA models mainly catalyze CO formation *via* a redox pathway involving oxygen vacancies where adsorbed CO<sub>2</sub> dissociates followed by CO desorption and water formation. The higher barriers for hydrogenation of formate intermediates compared to the overall barrier for the rWGS reaction explain the negligible CH<sub>3</sub>OH selectivity.

Received 16th February 2023,  
Accepted 17th July 2023

DOI: 10.1039/d3cy00222e

rsc.li/catalysis

## Introduction

The reduction of CO<sub>2</sub> emissions has become a crucial technological challenge because of the negative impact on the climate.<sup>1–3</sup> To address this challenge, the conversion of CO<sub>2</sub> captured from combustion processes and, in the future, directly from the air into liquid fuels and chemicals presents a viable solution, thereby reducing emissions and closing the carbon cycle. One of the most promising pathways for obtaining valuable products from CO<sub>2</sub> is *via* its hydrogenation, provided that the required hydrogen is obtained from renewable resources.<sup>4–6</sup> Not only does the large-scale hydrogenation of CO<sub>2</sub> into fuels offer an opportunity to decrease our reliance on fossil fuels for energy, this technology can also be leveraged to obtain chemical intermediates.<sup>7–10</sup> In this context, methanol is particularly attractive, because it can be used as a fuel or chemical building block.<sup>11–13</sup>

Currently, large-scale methanol production is achieved by converting synthesis gas (CO/CO<sub>2</sub>/H<sub>2</sub>) over a Cu/ZnO/Al<sub>2</sub>O<sub>3</sub> catalyst at temperatures of 473–573 K and pressures of 50–100

bar.<sup>14</sup> Challenges arise however when CO<sub>2</sub> is hydrogenated instead of CO. The Cu-based catalyst shows significant activity for the reverse water-gas-shift reaction (rWGS), leading to the formation of unwanted CO.<sup>15</sup> Moreover, the catalyst suffers from sintering, resulting in slow deactivation.<sup>16,17</sup> Many efforts have been made to identify new catalyst formulations with improved performance for the hydrogenation of CO<sub>2</sub> to CH<sub>3</sub>-OH.<sup>18</sup> Recently, indium oxide (In<sub>2</sub>O<sub>3</sub>) has emerged as a promising catalyst for CO<sub>2</sub> hydrogenation to methanol.<sup>19,20</sup> Several density functional theory (DFT) studies emphasize the role of oxygen vacancies in the mechanism of CO<sub>2</sub> hydrogenation to methanol on In<sub>2</sub>O<sub>3</sub>.<sup>19,21–25</sup> Although such catalysts enable high selectivity to methanol by suppressing the competitive rWGS reaction, CO<sub>2</sub> conversion is limited by the intrinsically low activity in H<sub>2</sub> activation. To improve this, the use of metal promoters has been investigated. Recently, we reported by microkinetic modelling that small Ni clusters on In<sub>2</sub>O<sub>3</sub> mainly catalyse methanol formation, whereas single atoms of Ni either doped in or adsorbed on In<sub>2</sub>O<sub>3</sub> mainly catalyse CO.<sup>26,27</sup> In a recent study, Pinheiro Araújo *et al.* reported that, atomically dispersed metal atoms (Pd, Pt, Rh, Ni, Co, Au, Ir) on the In<sub>2</sub>O<sub>3</sub> surface promote hydrogen activation and methanol production while hindering CO formation.<sup>28</sup> Frei *et al.* suggested by DFT calculations that single Ni atoms on In<sub>2</sub>O<sub>3</sub> could catalyse the rWGS reaction but not methanol synthesis.<sup>29</sup> The same authors proposed that single atoms of Pd doped in In<sub>2</sub>O<sub>3</sub> can stabilize Pd clusters on the In<sub>2</sub>O<sub>3</sub> surface, which can enhance H<sub>2</sub> activation and, therefore, CH<sub>3</sub>OH productivity.<sup>30</sup> Han *et al.* suggested that single atom (SA) of Pt

Laboratory of Inorganic Materials and Catalysis, Department of Chemical Engineering and Chemistry, Eindhoven University of Technology, 5600 MB Eindhoven, The Netherlands. E-mail: [i.a.w.filot@tue.nl](mailto:i.a.w.filot@tue.nl)

† Electronic supplementary information (ESI) available: Description of the structure of SA-In<sub>2</sub>O<sub>3</sub> models and oxygen vacancy formation (section S1–S3), geometries of elementary reaction steps (section S4–S7) full DFT dataset (section S8), and further microkinetic and DFT results (section S9 and S10). See DOI: <https://doi.org/10.1039/d3cy00222e>



doped in  $\text{In}_2\text{O}_3$  would result in high methanol selectivity, whereas Pt nanoparticles on  $\text{In}_2\text{O}_3$  would improve the rWGS reaction.<sup>31</sup> Sun *et al.* showed by DFT calculations that the energetically most favourable pathway for methanol synthesis on a  $\text{Pt}_4/\text{In}_2\text{O}_3$  model occurs *via* hydrogenation of a CO intermediate.<sup>32</sup> Wang *et al.* reported that highly dispersed Rh phases on  $\text{In}_2\text{O}_3$  can enhance dissociative  $\text{H}_2$  adsorption and oxygen vacancy formation.<sup>33</sup> Dostagir *et al.* found that Rh doped into  $\text{In}_2\text{O}_3$  catalyzes  $\text{CO}_2$  hydrogenation to formate species.<sup>34</sup> Furthermore, earlier DFT works pointed out that SAs on the  $\text{In}_2\text{O}_3$  surface do not catalyze the formation of  $\text{CH}_4$ .<sup>28–30,35,36</sup> In nearly all these studies, the formation of atomically dispersed metal atoms was effective in shifting the selectivity towards the desired product. Although the role of supported clusters in metal-promoted  $\text{In}_2\text{O}_3$  catalysts has been clarified for many cases,<sup>32,37</sup> generic understanding about the role of SAs is still lacking. Gaining a comprehensive understanding of the reaction pathways involved in the hydrogenation of  $\text{CO}_2$  to synthesize methanol requires a thorough investigation of the role of SAs in  $\text{In}_2\text{O}_3$ .

In the present work, we study the reaction mechanism of  $\text{CO}_2$  hydrogenation to  $\text{CH}_3\text{OH}$  and CO on SA- $\text{In}_2\text{O}_3$  model catalysts. Considering relevant literature, we have identified Ni, Pd, Pt, and Rh as potential promoters.<sup>28–31,34</sup> The reaction pathways explored in our DFT studies include a direct route for  $\text{CO}_2$  hydrogenation to methanol (formate pathway), a pathway to methanol *via* CO hydrogenation and the competing rWGS reaction (both direct and hydrogen-assisted). We performed DFT calculations to determine the reaction energetics for all elementary reaction steps, which serve as input for microkinetic modelling. Microkinetic simulations show that the SA- $\text{In}_2\text{O}_3$  model surfaces produce CO as the main product with a very low methanol selectivity. The observed outcome can be primarily attributed to the presence of oxygen vacancies, which enable the adsorption of  $\text{CO}_2$  and prompt activation towards facile direct C–O bond scission. In contrast, the formation of methanol is hampered by the high activation energies associated with the hydrogenation of formate intermediates, resulting in relatively low rates for the preferred methanol product.

## Computational methods

### Density functional theory calculations

The calculations reported in this work were done in the same manner as reported before.<sup>26,27</sup> All DFT calculations were conducted using the projector augmented wave (PAW) method<sup>38</sup> and the Perdew–Burke–Ernzerhof (PBE)<sup>39</sup> exchange–correlation functional as implemented in the Vienna *ab initio* simulation package (VASP) code.<sup>40,41</sup> The valence 5s and 5p states of In were treated explicitly as valence states within the scalar-relativistic PAW approach. By using a plane-wave basis set with a cut-off energy of 400 eV solutions to the Kohn–Sham equations were calculated. All calculations were spin-polarized. The Brillouin zone was sampled using a  $3 \times 3 \times 1$  Monkhorst-Pack grid. By using Gaussian smearing with a

smearing width ( $\sigma$ ) of 0.1 eV electron smearing was employed. The stoichiometric  $\text{In}_2\text{O}_3(111)$  surface was modelled as a 2D slab with periodic boundary conditions. To avoid the spurious interaction with neighbouring super cells, a 15.0 Å vacuum region was introduced in the *c*-direction. It was verified that the electron density approached zero at the edges of the periodic super cell in the *c*-direction. The bottom two layers were frozen, while the top two layers were allowed to perturb in all calculations. The supercell has dimensions of 14.57 Å  $\times$  14.57 Å  $\times$  26.01 Å. The  $\text{In}_2\text{O}_3(111)$  slab consisted of 96 O atoms and 64 In atoms, distributed in four atomic layers on top of which the SA species were placed.

The stable states of the elementary reaction steps pertaining to  $\text{CO}_2$  hydrogenation were calculated using the conjugate-gradient algorithm. Eqn (1) defines the adsorption energies of adsorbates ( $\Delta E_{\text{X}}^{\text{ads}}$ ):

$$\Delta E_{\text{X}}^{\text{ads}} = E_{\text{X+In}_2\text{O}_3(111)} - E_{\text{In}_2\text{O}_3(111)} - E_{\text{X}} \quad (1)$$

where  $E_{\text{X+In}_2\text{O}_3(111)}$  is the electronic energy of the catalyst plus adsorbate system,  $E_{\text{In}_2\text{O}_3(111)}$  is the reference energy of the  $\text{In}_2\text{O}_3(111)$  slab and  $E_{\text{X}}$  is the DFT-calculated energy of the adsorbate in the gas phase.

The influence of oxygen vacancies on the reaction energetics was investigated by removing oxygen atoms from the  $\text{In}_2\text{O}_3(111)$  lattice. Since oxygen vacancies in chemical reactors are formed *via* surface reduction by  $\text{H}_2$ , the energy required to remove an oxygen from  $\text{In}_2\text{O}_3$  ( $\Delta E_{\text{OV}}$ ) was calculated using  $\text{H}_2\text{O}$  as reference, according to the following equation

$$\Delta E_{\text{OV}} = E_{\text{defective slab}} - E_{\text{stoichiometric slab}} + E_{\text{H}_2\text{O}} - E_{\text{H}_2} \quad (2)$$

where  $E_{\text{defective slab}}$  is the electronic energy of the catalyst containing one oxygen vacancy,  $E_{\text{stoichiometric slab}}$  is the reference energy of the stoichiometric slab.  $E_{\text{H}_2\text{O}}$  and  $E_{\text{H}_2}$  are the DFT-calculated energies of gas-phase  $\text{H}_2\text{O}$  and  $\text{H}_2$ , respectively. Herein, we include the electronic energy, the zero-point energy correction and a finite temperature correction of translational and rotational energy of each gas-phase molecule.

Transition states were determined using the climbing-image nudged elastic band (CI-NEB) method.<sup>42</sup> A frequency analysis was performed to all states to verify that that stable states have no imaginary frequencies and transition states have a single imaginary frequency aligned with the reaction coordinate.<sup>43</sup> The Hessian matrix in this frequency analysis was constructed using a finite difference approach with a step size of 0.015 Å for displacement of individual atoms along each Cartesian coordinate. The normal mode vibrations found with these calculations were used to evaluate the zero-point energy (ZPE) correction and the vibrational partition functions.

Partial density of state (pDOS) analysis are conducted to analyze the electronic structure of each SA- $\text{In}_2\text{O}_3$  model using the Lobster package.<sup>44,45</sup> The atomic charges were calculated using the Bader charge method.<sup>46</sup>

## Microkinetic simulations

Microkinetic simulations were carried out based on the DFT-calculated activation and reaction energies. The kinetic network was modelled using a set of ordinary differential equations involving rate constants, surface coverages and partial pressures of gas-phase species. To integrate the differential equations with respect to time the linear multistep backwards differential formula method was employed with a relative and absolute tolerance of  $10^{-8}$ .<sup>47-49</sup>

The net rate of the adsorption process of a gas-phase species  $i$  was calculated as:

$$r_i = k_{i,\text{ads}}\theta^*P_i - k_{i,\text{des}}\theta_i \quad (3)$$

where  $\theta^*$  and  $\theta_i$  are the fraction of free sites and the fraction of coverage species  $i$ , respectively.  $k_{i,\text{ads/des}}$  is the rate constant for the adsorption/desorption process and  $P_i$  is the partial pressure of species  $i$ .

To model adsorption processes, we assumed that the adsorbate loses one translational degree of freedom in the transition state with respect to the initial state. As a result of this, the rate of adsorption derived from transition state theory is:

$$k_{i,\text{ads}} = \frac{PA_{\text{st}}}{\sqrt{2\pi m_i k_B T}}, \quad (4)$$

where  $A_{\text{st}}$  and  $m_i$  are the effective area of an adsorption site and the molar mass of the gas species, respectively.  $P$  and  $T$  are the total pressure and temperature, respectively, and  $k_B$  is the Boltzmann constant. To calculate the gas-phase entropy of the adsorbates we employed the thermochemical Shomate equation as given by

$$S^0 = A \cdot \ln(T) + B \cdot T + \frac{C \cdot T^2}{2} + \frac{D \cdot T^3}{3} - \frac{E}{2 \cdot T^2} + G, \quad (5)$$

where  $S^0$  is the standard molar entropy.<sup>50</sup> The parameters A-G from eqn (5) were obtained from the NIST Chemistry Webbook.<sup>51</sup> To model the desorption processes, we assumed that the desorbing species acquires two translational degrees of freedom and three rotational degrees of freedom in the transition state compared to the initial state. The resulting rate of desorption derived from transition state theory is:

$$k_{\text{des}} = \frac{k_B \cdot T^3}{h^3} \cdot \frac{A_{\text{st}}(2\pi m k_B)}{\sigma \theta_{\text{rot}}} \cdot e^{\frac{\Delta E_{\text{ads}}}{k_B T}}, \quad (6)$$

Herein,  $k_{\text{des}}$  is the rate constant for the desorption of the adsorbate,  $h$  is the Planck constant,  $\sigma$  is the symmetry number and is equal to 1,  $\theta_{\text{rot}}$  the rotational temperature, and  $\Delta E_{\text{ads}}$  the desorption energy. The value of  $A_{\text{st}}$  is equal to  $9 \times 10^{-19} \text{ m}^{-2}$ .

The rate constant ( $k$ ) of an elementary reaction step is given by the Eyring equation:

$$k = \frac{k_B T}{h} \frac{Q^{\#}}{Q} e^{\left(\frac{-\Delta E_{\text{act}}}{k_B T}\right)}, \quad (7)$$

where  $Q^{\#}$  and  $Q$  are the partition functions of the transition state and its corresponding initial state, respectively, and  $\Delta E_{\text{act}}$  is the ZPE-corrected activation energy.

We employed the concepts of the degree of rate control (DRC) developed by Kozuch and Shaik<sup>52,53</sup> and popularized by Campbell<sup>54</sup> as well as the degree of selectivity control (DSC)<sup>54-56</sup> to identify the steps that control the  $\text{CO}_2$  consumption rate and the product distribution.

Herein, the degree of rate control coefficient is defined as

$$X_{\text{RC},i} = \left( \frac{\partial \ln r_i}{\partial \ln k_i} \right)_{k_j \neq i, K_i} \quad (8)$$

A positive DRC coefficient indicates that the elementary reaction step is rate-controlling, whereas a negative coefficient corresponds to a rate-inhibiting elementary step.

## Results and discussion

### Structure of SA-In<sub>2</sub>O<sub>3</sub> models

To study the catalytic properties of single atoms (SAs) of Ni, Pd, Pt and Rh, we constructed four models in which the SA was placed on the In<sub>2</sub>O<sub>3</sub>(111) surface, which is the most stable termination of In<sub>2</sub>O<sub>3</sub>.<sup>57</sup> We first determined the most stable location of the SA on the In<sub>2</sub>O<sub>3</sub>(111) surface. For this, we calculated the adsorption energies of the SA in different positions (Table S1†). The most stable adsorption sites are depicted in Fig. 1. Single Ni, Pd and Pt atoms preferentially adsorb in bridge sites between two oxygen atoms, in agreement with previous theoretical studies (Fig. 1a-c).<sup>30,58</sup> The Rh SA prefers to coordinate to three oxygens (Fig. 1d). A partial density of states (pDOS) analysis of the SA-In<sub>2</sub>O<sub>3</sub> models shows that the bonding is mainly through interactions of the SA metal d orbitals and O 2p orbitals (Fig. S2†). The supported Ni, Pd, Pt and Rh SAs possess positive charges of +0.56, +0.35, +0.30 and +1.03, respectively. The energy needed to remove the SA atom to infinite distance from the surface is reported in Table S1.† Ni is most strongly bound to the surface ( $E_{\text{ads}} = -512 \text{ kJ mol}^{-1}$ ), followed by Pt ( $E_{\text{ads}} = -481 \text{ kJ mol}^{-1}$ ), Rh ( $E_{\text{ads}} = -425 \text{ kJ mol}^{-1}$ ) and Pd ( $E_{\text{ads}} = -339 \text{ kJ mol}^{-1}$ ). To understand the mobility of SAs on the In<sub>2</sub>O<sub>3</sub>(111) surface, we determined the barrier for migration between stable adsorption sites (Table S2†). Surface migration of SAs is associated with relatively high barriers for Ni, Pd and Rh ( $E_a > 100 \text{ kJ mol}^{-1}$ ), whereas much lower barriers are found for Pd ( $E_a < 50 \text{ kJ mol}^{-1}$ ). This is in line with the weaker binding energy of Pd with the In<sub>2</sub>O<sub>3</sub>(111) surface compared to Pt, Ni and Rh.

### Oxygen vacancy formation

Oxygen vacancies (Ov) in the In<sub>2</sub>O<sub>3</sub> surface have been identified as the active sites for  $\text{CO}_2$  hydrogenation.<sup>19,21,22</sup> Here, we determine the effect of surface SAs on the formation of such vacancies. To this purpose, we calculate the energy required to remove an oxygen atom on each SA-In<sub>2</sub>O<sub>3</sub> model and compare the results with data for bare In<sub>2</sub>O<sub>3</sub> (Fig. 2),

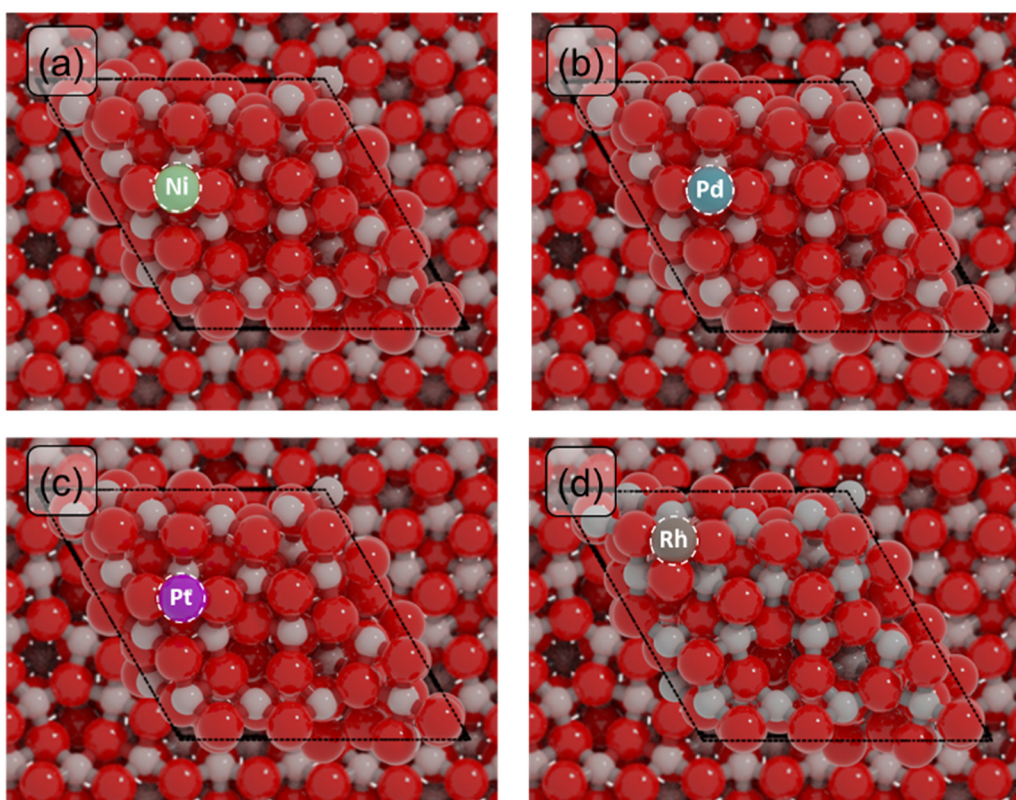


**Fig. 1** Structural models used in DFT calculations composed of single atoms on the  $\text{In}_2\text{O}_3(111)$  surface. (a)  $\text{Ni}-\text{In}_2\text{O}_3$ , (b)  $\text{Pd}-\text{In}_2\text{O}_3$ , (c)  $\text{Pt}-\text{In}_2\text{O}_3$  and (d)  $\text{Rh}-\text{In}_2\text{O}_3$ . (green: Ni, light blue: Pd, purple: Pt; brown: Rh; red: O; grey: In).

Table S3 and Fig. S3†). Since oxygen vacancies during  $\text{CO}_2$  hydrogenation are formed *via* surface reduction by  $\text{H}_2$ , the computed energies are referenced to gaseous  $\text{H}_2\text{O}$ . For the bare  $\text{In}_2\text{O}_3(111)$  surface (Fig. 2a), the energy needed to remove an oxygen atom ( $E_{\text{ov}}$ ) ranges between  $-61$  and  $8 \text{ kJ mol}^{-1}$ , in line with previous theoretical calculations.<sup>59</sup> The presence of a Ni atom on  $\text{In}_2\text{O}_3$  (Fig. 2b) significantly increases the oxygen vacancy formation energy, resulting in  $E_{\text{ov}}$  values between  $139$  and  $190 \text{ kJ mol}^{-1}$ . The effect of a Pd SA is much less pronounced, resulting in values for  $E_{\text{ov}}$  comparable to those for the bare  $\text{In}_2\text{O}_3(111)$  surface, namely between  $-77$  and  $80 \text{ kJ mol}^{-1}$ . For the  $\text{Pt}-\text{In}_2\text{O}_3$  case (Fig. 2d),  $E_{\text{ov}}$  assumes higher values than for Pd ranging between  $-35$  and  $217 \text{ kJ mol}^{-1}$ . The  $\text{Rh}-\text{In}_2\text{O}_3$  model (Fig. 2e) has intermediate values for  $E_{\text{ov}}$  ranging between  $39$  and  $170 \text{ kJ mol}^{-1}$ . Overall, the removal of an oxygen atom on the bare  $\text{In}_2\text{O}_3(111)$  surface is less energetically demanding in comparison to SA- $\text{In}_2\text{O}_3$  models, except for Pd, where the oxygen formation energy is very similar.

Further inspection of Fig. 2b–d shows that, for each of the SA-promoted surfaces, formation of vacancies is easier for lattice oxygen atoms directly bonding to the SA than for O atoms bonding only to In atoms. Comparing the  $\text{H}_2\text{O}$ -referenced  $E_{\text{ov}}$  values for O binding to the SA, we computed as lowest lowest  $E_{\text{ov}}$  values of  $141$ ,  $-71$ ,  $-35$  and  $39 \text{ kJ mol}^{-1}$  for Ni-, Pd-, Pd- and Rh- $\text{In}_2\text{O}_3$ , respectively (Table S4†). On bare  $\text{In}_2\text{O}_3$ , the lowest  $E_{\text{ov}}$  value is  $-61 \text{ kJ mol}^{-1}$ . The relatively

more endothermic  $E_{\text{ov}}$  values for Ni-, Pt- and Rh- $\text{In}_2\text{O}_3$  are in line with the strong adsorption energy of the SA on the surface (Table S1†). Because Pd binds to the surface less strongly,  $E_{\text{ov}}$  is relatively speaking more exothermic than for the other SAs. To understand whether oxygen vacancies will be formed on these models under reaction conditions and what role they play in  $\text{CO}_2$  hydrogenation, we study the mechanism of oxygen vacancy formation *via* surface reduction by  $\text{H}_2$  as well as the  $\text{CO}_2$  hydrogenation reaction pathways by means of microkinetic simulations (*vide infra*).

### Reaction mechanism

We performed DFT calculations to determine the reaction mechanism of  $\text{CO}_2$  hydrogenation to methanol ( $\text{CH}_3\text{OH}$ ), carbon monoxide ( $\text{CO}$ ) and water ( $\text{H}_2\text{O}$ ). Hydrogenation of  $\text{CO}_2$  to methane ( $\text{CH}_4$ ) was not included, because methane formation was not observed in experiments with low-loaded metal-promoted  $\text{In}_2\text{O}_3$  catalysts.<sup>28,32,34</sup> Furthermore, earlier DFT works pointed out that SAs on the  $\text{In}_2\text{O}_3$  surface do not catalyse the formation of  $\text{CH}_4$ .<sup>28–30,35</sup> The mechanism is depicted in Fig. 3 in the form of a reaction network diagram. Following previous computational studies, we investigated the pathways for (i) the formation of oxygen vacancies through  $\text{H}_2\text{O}$  formation, (ii) the formation of  $\text{CH}_3\text{OH}$  *via* formate, and (iii) the reverse water-gas shift (rWGS) pathway leading to  $\text{CO}_2$ .<sup>32,57,60–62</sup> The latter rWGS reaction can take



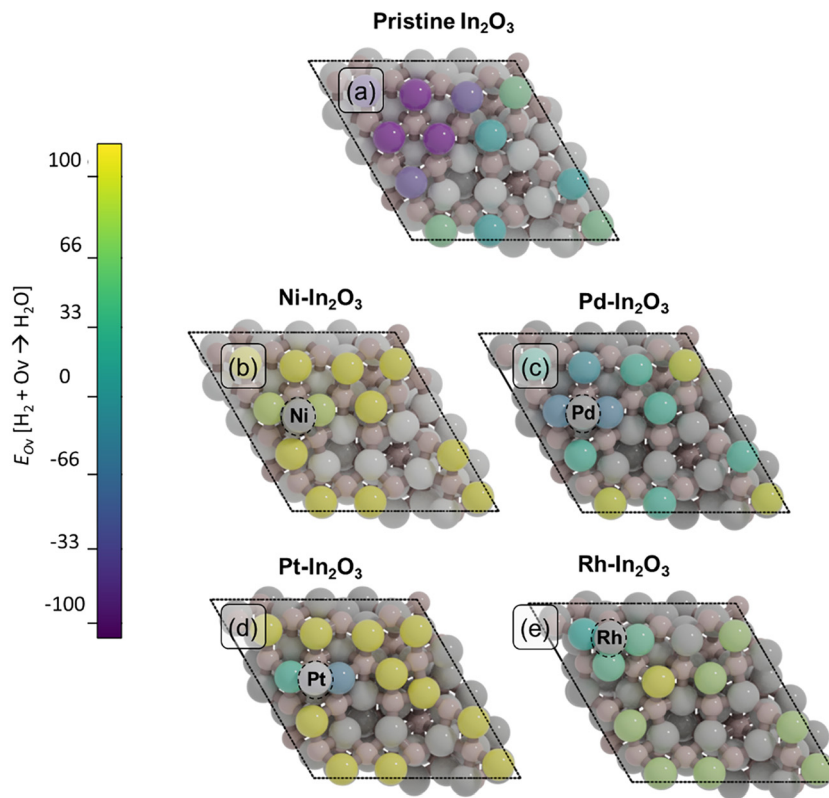


**Fig. 2** Oxygen vacancy formation energies ( $E_{\text{Ov}}$ ,  $\text{kJ mol}^{-1}$ ) for the 12 surface oxygens on (a) bare  $\text{In}_2\text{O}_3$ , (b)  $\text{Ni-In}_2\text{O}_3$ , (c)  $\text{Pd-In}_2\text{O}_3$ , (d)  $\text{Pt-In}_2\text{O}_3$ , and (e)  $\text{Rh-In}_2\text{O}_3$ . The coloring of the 12 surface oxygen atoms corresponds to their  $E_{\text{Ov}}$  indicated in the color bar. Vacancy formation energies are given with respect to  $\text{H}_2\text{O}$  formation. All other atoms are colored in grey. The SAs are highlighted inside dashed circles.

place *via* either direct C–O bond cleavage in adsorbed CO or an H-assisted pathway involving COOH intermediate. In addition to methanol formation *via* formate, we considered the direct hydrogenation pathway of CO intermediate into  $\text{CH}_3\text{OH}$ . We included a comparison with the DFT results of Frei *et al.* on  $\text{In}_2\text{O}_3(111)$ .<sup>57</sup> Fig. 4 depicts the potential energy diagrams (PED) for each of these routes.

Next, we discuss the elementary reaction steps on each SA- $\text{In}_2\text{O}_3$  surface and highlight differences in activation energies and transition-state structures. The activation barriers are given with respect to the most stable adsorbed state for each intermediate.

The geometries corresponding to initial, transition and final states can be found in the ESI† (Tables S6–S9). The computed forward and backward barriers for all elementary reaction steps are given in Tables S10–S13.†

### Oxygen vacancy formation

We first discuss the formation of oxygen vacancies (steps 1–3). On all SA- $\text{In}_2\text{O}_3$  surfaces, the oxygen corresponding to the lowest  $E_{\text{Ov}}$  value is removed. For Ni-, Pd and Pt- $\text{In}_2\text{O}_3$ , this corresponds to forming an oxygen vacancy in position  $\text{O}_{\text{v}3}$  (Table S2 and Fig. S3†). For Rh- $\text{In}_2\text{O}_3$  formation of an oxygen vacancy in position  $\text{O}_{\text{v}2}$  is preferred. On all SA- $\text{In}_2\text{O}_3$  models,  $\text{H}_2$  is heterolytically dissociated into SA–H and O–H moieties

(step 1). Hydrogen activation is facile on  $\text{Ni-In}_2\text{O}_3$  ( $E_{\text{act},\text{Ni}} = 19 \text{ kJ mol}^{-1}$ ) and more difficult on Pd-, Pt- and Rh- $\text{In}_2\text{O}_3$  ( $E_{\text{act},\text{Pd}} = 62 \text{ kJ mol}^{-1}$ ,  $E_{\text{act},\text{Pt}} = 48 \text{ kJ mol}^{-1}$  and  $E_{\text{act},\text{Rh}} = 57 \text{ kJ mol}^{-1}$ ). Dissociative adsorption of  $\text{H}_2$  is more exothermic on Pt- and Rh- $\text{In}_2\text{O}_3$  ( $\Delta E_{\text{r},\text{Pt}} = -94 \text{ kJ mol}^{-1}$ ,  $\Delta E_{\text{r},\text{Rh}} = -144 \text{ kJ mol}^{-1}$ ) than on Ni- and Pd- $\text{In}_2\text{O}_3$  ( $\Delta E_{\text{r},\text{Ni}} = -36 \text{ kJ mol}^{-1}$ ,  $\Delta E_{\text{r},\text{Pd}} = -10 \text{ kJ mol}^{-1}$ ). Oxygen vacancy formation proceeds *via* proton migration from a SA–H to an O–H moiety, resulting in adsorbed  $\text{H}_2\text{O}$  (step 2). This step has similar barriers for  $\text{Ni-In}_2\text{O}_3$ , Pt- $\text{In}_2\text{O}_3$  and Rh- $\text{In}_2\text{O}_3$  ( $E_{\text{act},\text{Ni}} = 93 \text{ kJ mol}^{-1}$ ,  $E_{\text{act},\text{Pt}} = 68 \text{ kJ mol}^{-1}$  and  $E_{\text{act},\text{Rh}} = 76 \text{ kJ mol}^{-1}$ ). On these models, this step is endothermic by 27, 69, and 27  $\text{kJ mol}^{-1}$ , respectively. The lowest barrier is obtained for Pd- $\text{In}_2\text{O}_3$  ( $E_{\text{act}} = 47 \text{ kJ mol}^{-1}$ ,  $\Delta E_{\text{r}} = 80 \text{ kJ mol}^{-1}$ ).  $\text{H}_2\text{O}$  desorption completes the oxygen vacancy formation pathway (step 3). The highest desorption energy is computed on  $\text{Ni-In}_2\text{O}_3$  ( $\Delta E_{\text{des},\text{Ni}} = 177 \text{ kJ mol}^{-1}$ ), while this step is considerably easier on the other SA models ( $\Delta E_{\text{des},\text{Pd}} = 12 \text{ kJ mol}^{-1}$ ,  $\Delta E_{\text{des},\text{Pt}} = 41 \text{ kJ mol}^{-1}$  and  $\Delta E_{\text{des},\text{Rh}} = 26 \text{ kJ mol}^{-1}$ ). The overall reaction energy for oxygen vacancy formation with respect to gas-phase  $\text{H}_2$  amounts to  $+150 \text{ kJ mol}^{-1}$  (Ni),  $-72 \text{ kJ mol}^{-1}$  (Pd),  $-41 \text{ kJ mol}^{-1}$  (Pt) and  $+16 \text{ kJ mol}^{-1}$  (Rh). The overall barriers with respect to gas-phase  $\text{H}_2$  are 150, 72, 48 and 57  $\text{kJ mol}^{-1}$  for Ni-, Pd-, Pt-, and Rh- $\text{In}_2\text{O}_3$ , respectively. Notably, the higher overall barrier for Ni is in line with the stronger Ni–O bond as compared to the more noble metals considered here (Table S14†). With respect to

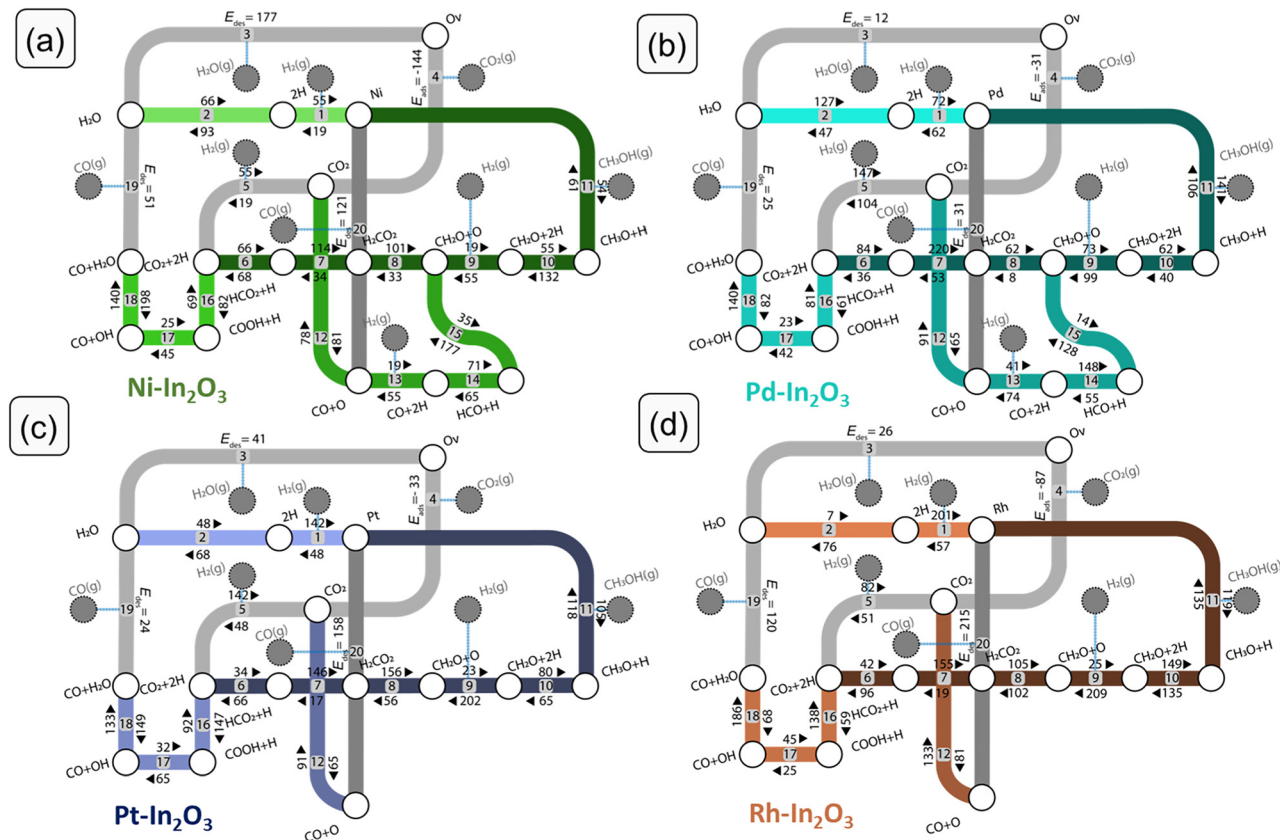


Fig. 3 Complete reaction networks of  $\text{CO}_2$  hydrogenation to  $\text{CO}$  and  $\text{CH}_3\text{OH}$  for (a) Ni-, (b) Pd-, (c) Pt- and (d)  $\text{Rh-In}_2\text{O}_3$ . Each elementary step is numbered. The forward and backward reaction energies, as well as the adsorption and desorption energies are given in  $\text{kJ mol}^{-1}$ .

the same reference, the unpromoted  $\text{In}_2\text{O}_3(111)$  surface has an overall barrier for oxygen vacancy formation of  $67 \text{ kJ mol}^{-1}$ .<sup>59,63</sup> The adsorption configurations of the SA on the  $\text{In}_2\text{O}_3(111)$  surface after formation of an oxygen vacancy are reported in Fig. S4.<sup>†</sup>

#### Methanol synthesis *via* formate

For  $\text{CO}_2$  hydrogenation, we first discuss the most stable adsorption configuration for  $\text{CO}_2$  on the SA- $\text{In}_2\text{O}_3$  models. We have explored different adsorption configurations of  $\text{CO}_2$  on the SA- $\text{In}_2\text{O}_3$  models. The results are reported in Table S5 and Fig. S5,<sup>†</sup> respectively. On Ni-, Pd- and Pt- $\text{In}_2\text{O}_3$   $\text{CO}_2$  adsorbs near the SA with one of its O atoms occupying the oxygen vacancy and the C atom bonding to the SA. On Rh- $\text{In}_2\text{O}_3$ , the C atom coordinates directly to a lattice O instead of the SA. The adsorption energies of  $\text{CO}_2$  are  $-144$ ,  $-31$ ,  $-33$  and  $-87 \text{ kJ mol}^{-1}$  for Ni-, Pd-, Pt- and Rh- $\text{In}_2\text{O}_3$ , respectively. Thus, the interaction of  $\text{CO}_2$  with Ni and Rh is relatively strong compared to Pd and Pt. This is in line with trends found in a previous computational study for  $\text{CO}_2$  adsorption on low-index surfaces of transition metals.<sup>64</sup>

Dissociative adsorption of  $\text{H}_2$  (step 5) is heterolytic on all SA- $\text{In}_2\text{O}_3$  models and leads to O-H and SA-H moieties adjacent to adsorbed  $\text{CO}_2$ . Homolytic dissociation on top of the metal atom was also investigated but resulted in the

formation of a SA-H and a O-H moiety. This state constitutes the initial configuration for  $\text{CO}_2$  hydrogenation. Dissociative adsorption is facile on Ni- $\text{In}_2\text{O}_3$  ( $E_{\text{act},\text{Ni}} = 19 \text{ kJ mol}^{-1}$ ), whereas higher barriers were computed for Pd-, Pt- and Rh- $\text{In}_2\text{O}_3$  ( $E_{\text{act},\text{Pd}} = 104 \text{ kJ mol}^{-1}$ ,  $E_{\text{act},\text{Pt}} = 48 \text{ kJ mol}^{-1}$ ,  $E_{\text{act},\text{Rh}} = 51 \text{ kJ mol}^{-1}$ ). Next, methanol can be obtained *via* a mechanism involving a formate intermediate (steps 6–11 in Fig. 3). The PEDs of the formate pathway for the SA- $\text{In}_2\text{O}_3$  models are reported in Fig. 4a. The C atom in  $\text{CO}_2$  is hydrogenated by a SA-H to  $\text{HCO}_2$  (step 6). The forward activation energies for Ni-, Pd-, Pt- and Rh- $\text{In}_2\text{O}_3$  are respectively  $66$ ,  $84$ ,  $34$  and  $42 \text{ kJ mol}^{-1}$ . This reaction is endothermic for Pd-, Pt- and Rh- $\text{In}_2\text{O}_3$  with reaction energies of  $48$ ,  $32$  and  $54 \text{ kJ mol}^{-1}$  and slightly exothermic for Ni- $\text{In}_2\text{O}_3$  ( $\Delta E_r = -2 \text{ kJ mol}^{-1}$ ). The C atom in  $\text{HCO}_2$  is protonated again *via* migration of a O-H to a SA-H moiety, resulting in  $\text{H}_2\text{CO}_2$  (step 7). Forming the  $\text{H}_2\text{CO}_2$  intermediate from  $\text{HCO}_2$  is endothermic on all SA- $\text{In}_2\text{O}_3$  models and involves relatively high activation energies of  $114$ ,  $220$ ,  $146$ , and  $155 \text{ kJ mol}^{-1}$  for Ni-, Pd-, Pt- and Rh- $\text{In}_2\text{O}_3$ , respectively. Notably, higher barriers are associated with migration from O-H to SA-H compared to direct hydrogenation of the C atom by a SA-A moiety. Furthermore, step 7 is the most difficult one in the formate pathway for all SAs. Direct migration of a O-H to hydrogenate the C atom in  $\text{HCO}_2$  was not considered, as it will lead to even higher barriers. Next, scission of one of the C-O bonds in the  $\text{H}_2\text{CO}_2$



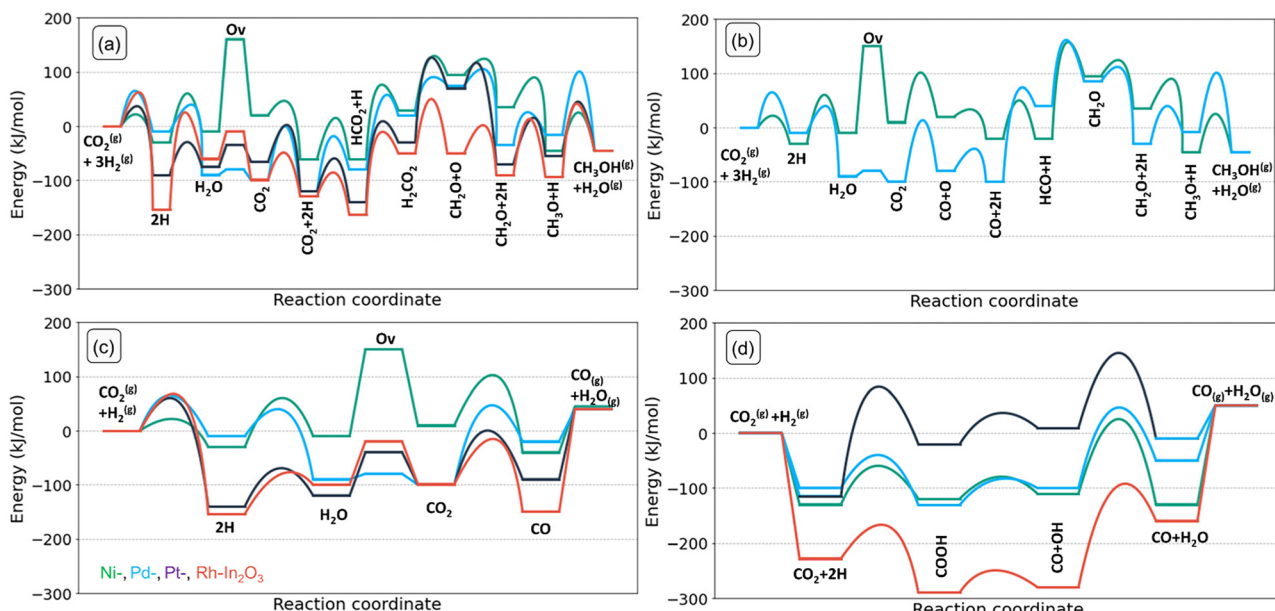


**Fig. 4** Potential energy diagrams of (a) formate pathway to  $\text{CH}_3\text{OH}$ , (b) CO hydrogenation pathway to  $\text{CH}_3\text{OH}$  and (c) redox pathway to CO and (d) carboxyl pathway to CO on different models.

intermediate results in  $\text{CH}_2\text{O}$  and O (step 8). This step leads to healing of the oxygen vacancy. This step is endothermic for Ni-, and Pd- and Pt- and  $\text{Pt-In}_2\text{O}_3$  surfaces with reaction energies of 68, 54 and 100  $\text{kJ mol}^{-1}$ , respectively, whereas it is slightly exothermic for  $\text{Rh-In}_2\text{O}_3$  ( $\Delta E_r = -3 \text{ kJ mol}^{-1}$ ). Furthermore, lower barriers are found for Pd- ( $E_{\text{act}} = 62 \text{ kJ mol}^{-1}$ ) than for Ni- ( $E_{\text{act}} = 101 \text{ kJ mol}^{-1}$ ), Pt- ( $E_{\text{act}} = 156 \text{ kJ mol}^{-1}$ ) and  $\text{Rh-In}_2\text{O}_3$  ( $E_{\text{act}} = 105 \text{ kJ mol}^{-1}$ ). Another pathway preceding C–O bond scission involves hydrogenation of  $\text{HCO}_2$  to  $\text{HCO}_2\text{H}$ . We could not find a TS for this reaction because of the very weak adsorption of  $\text{HCO}_2\text{H}$ . A similar issue was encountered in investigating the hydrogenation of  $\text{H}_2\text{CO}_2$  to  $\text{H}_2\text{CO}_2\text{H}$ . On all  $\text{SA-In}_2\text{O}_3$  models, dissociative adsorption of another  $\text{H}_2$  leads to a SA–H and O–H moieties adsorbed next to  $\text{CH}_2\text{O}$  (step 9). The  $\text{CH}_2\text{O}$  moiety resulting from  $\text{H}_2\text{CO}_2$  dissociation is then hydrogenated to  $\text{CH}_3\text{O}$  by proton migration from a SA–H moiety (step 10). This step has an activation energy of 55, 62, 80 and 149  $\text{kJ mol}^{-1}$  for Ni-, Pd- Pt, and  $\text{Rh-In}_2\text{O}_3$ , respectively. Furthermore, it is endothermic for Pd-, Pt and  $\text{Rh-In}_2\text{O}_3$  ( $E_{\text{act,Pd}} = 18 \text{ kJ mol}^{-1}$ ,  $E_{\text{act,Pt}} = 15 \text{ kJ mol}^{-1}$ ,  $E_{\text{act,Rh}} = 14 \text{ kJ mol}^{-1}$ ), exothermic for  $\text{Ni-In}_2\text{O}_3$  ( $E_{\text{act,Ni}} = -77 \text{ kJ mol}^{-1}$ ). Finally,  $\text{CH}_3\text{OH}$  is obtained in a single concerted step from  $\text{CH}_3\text{O}$  via proton migration from the OH (step 11). This elementary reaction step has activation energies of 61, 106, 118 and 135  $\text{kJ mol}^{-1}$  for Ni-, Pd- Pt, and  $\text{Rh-In}_2\text{O}_3$ , respectively. Furthermore, it is moderately exothermic for Ni-, Pd- and  $\text{Pt-In}_2\text{O}_3$  ( $\Delta E_{\text{r,Ni}} = -7 \text{ kJ mol}^{-1}$ ,  $\Delta E_{\text{r,Pd}} = -35 \text{ kJ mol}^{-1}$ ,  $\Delta E_{\text{r,Pt}} = -13 \text{ kJ mol}^{-1}$ ), slightly endothermic for  $\text{Rh-In}_2\text{O}_3$  ( $\Delta E_{\text{r,Rh}} = 16 \text{ kJ mol}^{-1}$ ).

Frei *et al.* speculated based on potential energy diagrams that the most energetically favourable path to methanol involves three consecutive additions of hydrides and protons and features  $\text{HCO}_2\text{H}$  and  $\text{CH}_2(\text{OH})_2$  as intermediates.<sup>57</sup>

However, as pointed out earlier, the very weak adsorption of  $\text{HCO}_2\text{H}$  precludes this pathway on the  $\text{SA-In}_2\text{O}_3$  models we investigated.

**Methanol synthesis via CO.** The presence of metal atoms on the surface of  $\text{In}_2\text{O}_3$  can allow for methanol formation *via* CO hydrogenation, which does not take place on unpromoted  $\text{In}_2\text{O}_3$ .<sup>23</sup> We thus included this pathway and show the corresponding PEDs in Fig. 4b. After formation of an oxygen vacancy (steps 1–3) and  $\text{CO}_2$  adsorption (step 4), direct C–O bond scission can take place (step 12). This step leads to healing of the oxygen vacancy and adsorbed CO and has activation energies of 91, 65, 65 and 81  $\text{kJ mol}^{-1}$  for Ni-, Pd- Pt, and  $\text{Rh-In}_2\text{O}_3$ , respectively. Furthermore, it is exothermic for Pd-, Pt- and  $\text{Rh-In}_2\text{O}_3$  with reaction energy of -26, -26 and -52, respectively, while it is slightly endothermic for  $\text{Ni-In}_2\text{O}_3$  ( $\Delta E_{\text{r,Ni}} = 9 \text{ kJ mol}^{-1}$ ). In the final state, the resulting CO moiety is linearly adsorbed on the SA (SA–C distances: 1.73 Å (Ni), 1.85 Å (Pd), 1.82 Å (Pt) and 1.82 Å (Rh), while the O atom from  $\text{CO}_2$  is used to heal the oxygen vacancy in the  $\text{In}_2\text{O}_3$  surface. We did not find a TS for the two subsequent hydrogenation steps from CO to HCO and  $\text{H}_2\text{CO}$  for Pt- and  $\text{Rh-In}_2\text{O}_3$ . Accordingly, we only report methanol formation *via* CO for Ni- and Pd- $\text{In}_2\text{O}_3$ .

For Ni- and Pd- $\text{In}_2\text{O}_3$ ,  $\text{H}_2$  is heterolytically dissociated into a SA–H and an O–H moiety (step 13). Such mode of dissociative adsorption of  $\text{H}_2$  is more facile on  $\text{Ni-In}_2\text{O}_3$  ( $E_{\text{act,Ni}} = 19 \text{ kJ mol}^{-1}$ ) than on Pd- $\text{In}_2\text{O}_3$  ( $E_{\text{act,Pd}} = 41 \text{ kJ mol}^{-1}$ ). Such state where CO is adsorbed next to a SA–H and a O–H moiety constitutes the initial state of the CO hydrogenation pathway. CO hydrogenation to HCO proceeds using the H adsorbed on the SA (step 14) with activation energies of 71  $\text{kJ mol}^{-1}$  ( $\text{Ni-In}_2\text{O}_3$ ) and 148  $\text{kJ mol}^{-1}$  ( $\text{Pd-In}_2\text{O}_3$ ). In line with this difference, the reaction is much more endothermic for Pd ( $\Delta E_{\text{r,Pd}} = 93 \text{ kJ mol}^{-1}$ ) than for Ni ( $\Delta E_{\text{r,Ni}} = 6 \text{ kJ mol}^{-1}$ ).



Subsequently, HCO is hydrogenated to CH<sub>2</sub>O (step 15) with barriers of 177 kJ mol<sup>-1</sup> (Ni-In<sub>2</sub>O<sub>3</sub>) and 128 kJ mol<sup>-1</sup> (Pd-In<sub>2</sub>O<sub>3</sub>). We found that the preferential pathway involves migration of H from the OH moiety to the SA, followed by hydrogenation of HCO to CH<sub>2</sub>O. Direct migration of a OH to hydrogenate the C atom in HCO would face a higher barrier and was therefore not studied. This elementary step is endothermic for both SA-In<sub>2</sub>O<sub>3</sub> models ( $\Delta E_{r,Ni} = 142$ ,  $\Delta E_{r,Pd} = 114$  kJ mol<sup>-1</sup>, respectively). The resulting CH<sub>2</sub>O intermediate also occurs in the formate pathway to methanol discussed above. Thus, further hydrogenation of CH<sub>2</sub>O to methanol will occur *via* steps 9 and 10.

### CO formation *via* rWGS

On SA-In<sub>2</sub>O<sub>3</sub> models, the formation of CO can occur either *via* direct C–O bond cleavage of CO<sub>2</sub> (redox pathway, steps 4 and 20) or *via* a H-assisted pathway involving a COOH intermediate (carboxyl pathway, steps 16–19). In the redox pathway, after formation of H<sub>2</sub>O (steps 1–3) and CO<sub>2</sub> adsorption (step 4) one of the C–O bonds in CO<sub>2</sub> is cleaved (step 12). These steps have been previously discussed. The desorption of CO (step 20) closes the rWGS catalytic cycle. The highest barriers for CO desorption are found on Pt- ( $\Delta E_{des,Pt} = 158$  kJ mol<sup>-1</sup>) and Rh-In<sub>2</sub>O<sub>3</sub> ( $\Delta E_{des,Rh} = 215$  kJ mol<sup>-1</sup>) whereas lower values are found on Ni- ( $\Delta E_{des,Ni} = 121$  kJ mol<sup>-1</sup>) and Pd-In<sub>2</sub>O<sub>3</sub> ( $\Delta E_{des,Pd} = 31$  kJ mol<sup>-1</sup>). Concerning the unpromoted In<sub>2</sub>O<sub>3</sub>, Ye *et al.* reported that the process replenishing an oxygen vacancy by direct cleavage of the C–O bond in CO<sub>2</sub> has a barrier of 134 kJ mol<sup>-1</sup> on an In<sub>2</sub>O<sub>3</sub>(110) model surface.<sup>61</sup>

The carboxyl pathway proceeds by protonation of adsorbed CO<sub>2</sub> to form COOH by a SA–H moiety (step 16). The highest activation energies are computed for Ni-In<sub>2</sub>O<sub>3</sub> ( $E_{act} = 82$  kJ mol<sup>-1</sup>) and Pt-In<sub>2</sub>O<sub>3</sub> ( $E_{act} = 147$  kJ mol<sup>-1</sup>) followed by Pd-In<sub>2</sub>O<sub>3</sub> ( $E_{act} = 61$  kJ mol<sup>-1</sup>) and Rh-In<sub>2</sub>O<sub>3</sub> ( $E_{act} = 59$  kJ mol<sup>-1</sup>). Furthermore, this elementary step is endothermic for Ni- and Pt-In<sub>2</sub>O<sub>3</sub> ( $\Delta E_{r,Ni} = 74$  kJ mol<sup>-1</sup>,  $\Delta E_{r,Pt} = 55$  kJ mol<sup>-1</sup>), whereas it is exothermic for Pd- and Rh-In<sub>2</sub>O<sub>3</sub> ( $\Delta E_{r,Pd} = -20$  kJ mol<sup>-1</sup>,  $E_{r,Rh} = -78$  kJ mol<sup>-1</sup>). Formation a COOH intermediate is associated with higher barriers compared to formation of HCOO, in line with an earlier study on In<sub>2</sub>O<sub>3</sub>.<sup>65</sup> Next, COOH dissociates into CO and OH (step 17). This step features activation energies of 45, 42, 65, and 25 kJ mol<sup>-1</sup> for Ni-, Pd-, Pt- and Rh-In<sub>2</sub>O<sub>3</sub>, respectively. Furthermore, it is endothermic for all SA-In<sub>2</sub>O<sub>3</sub> surfaces ( $\Delta E_{r,Ni} = 17$  kJ mol<sup>-1</sup>,  $\Delta E_{r,Pd} = 19$  kJ mol<sup>-1</sup>,  $\Delta E_{r,Pt} = 33$  kJ mol<sup>-1</sup>, and  $\Delta E_{r,Rh} = 20$  kJ mol<sup>-1</sup>). Water is formed *via* proton transfer to the OH moiety obtained from COOH dissociation (step 18). This step features activation energies of 140, 140, 133 and 186 kJ mol<sup>-1</sup> for Ni-, Pd-, Pt- and Rh-In<sub>2</sub>O<sub>3</sub>, respectively. Moreover, it is endothermic for Rh-, and Pd-In<sub>2</sub>O<sub>3</sub> ( $\Delta E_{r,Rh} = 107$  kJ mol<sup>-1</sup>, and  $\Delta E_{r,Pd} = 58$  kJ mol<sup>-1</sup>), and exothermic for Ni- and Pt-In<sub>2</sub>O<sub>3</sub> ( $\Delta E_{r,Ni} = -58$  kJ mol<sup>-1</sup>, and  $\Delta E_{r,Pt} = -16$  kJ mol<sup>-1</sup>). Notably, this step features the highest activation energy of the carboxyl pathway for all SA-In<sub>2</sub>O<sub>3</sub>. The elementary step of COOH dissociation on the

bare In<sub>2</sub>O<sub>3</sub>(111) surface is associated with a relatively high barrier (146 kJ mol<sup>-1</sup>), similar to the ones found on our SA-In<sub>2</sub>O<sub>3</sub> models. Desorption of CO (step 19) features a barrier of 51, 25, 24 and 120 kJ mol<sup>-1</sup> for Ni-, Pd-, Pt- and Rh-In<sub>2</sub>O<sub>3</sub>, respectively, closing the carboxyl cycle.

### Microkinetic simulations

**Overall kinetics.** To compare the catalytic activities of the various SA-In<sub>2</sub>O<sub>3</sub> model surfaces, we calculate the CO<sub>2</sub> hydrogenation reaction rate using a microkinetic model based on DFT-computed reaction energetics. The active sites in our model consist of isolated single atoms, stabilized on the In<sub>2</sub>O<sub>3</sub> support. We do not take migration of intermediates between different active sites into account. In other words, co-adsorbed species are modelled as distinct variations of a single active site. In this approximation, all elementary reaction steps are unimolecular, with exception of the adsorption and desorption steps. A detailed list of the elementary reaction steps is provided in the ESI† (Tables S10–13).

The CO<sub>2</sub> consumption rate and CH<sub>3</sub>OH selectivity as a function of temperature for each SA-In<sub>2</sub>O<sub>3</sub> model are displayed in Fig. 5. The turnover frequencies (TOF) towards CH<sub>3</sub>OH and CO (TOF<sub>CH<sub>3</sub>OH</sub> and TOF<sub>CO</sub>, respectively) are reported in Fig. S6.† We also constructed a microkinetic model for unpromoted In<sub>2</sub>O<sub>3</sub> based on the published DFT data of Frei *et al.*<sup>57</sup> Fig. 5a shows that the CO<sub>2</sub> conversion rate decreases in the order Pd > Ni > Pt > Rh. Furthermore, none of the SA-In<sub>2</sub>O<sub>3</sub> models show any appreciable methanol selectivity (Fig. 5b), which is due to the much lower TOF<sub>CH<sub>3</sub>OH</sub> in comparison to TOF<sub>CO</sub> (Fig. S6c and d†).

Compared to bare In<sub>2</sub>O<sub>3</sub>, the adsorption of a SA on the In<sub>2</sub>O<sub>3</sub>(111) surface results in lower CO<sub>2</sub> consumption rates (Fig. S6a†) and TOF<sub>CH<sub>3</sub>OH</sub> for  $T < 300$  °C (Fig. S6c†). In the same range, the TOF<sub>CO</sub> decreases in the order Pd > Ni > bare In<sub>2</sub>O<sub>3</sub> > Pt > Rh (Fig. S6d†).

The analysis of the surface state, apparent activation energy and reaction orders as function of temperature is given in Fig. 6. The coverages in Fig. 6 should be interpreted as the fraction of time the system spends in a particular state (*i.e.*, the time average). According to the ergodicity principle in statistical thermodynamics, this equals the fraction of active sites that is in a particular state (*i.e.*, the ensemble average).

On the Ni-In<sub>2</sub>O<sub>3</sub> surface (Fig. 6a), the dominant surface state at lower temperatures features two adsorbed H species (2H). The reason behind this can be understood from Fig. 3a. Activation of H<sub>2</sub> and subsequent H<sub>2</sub>O formation (steps 1–2) are facile ( $E_{act} = 19$  kJ mol<sup>-1</sup> and  $E_{act} = 74$  kJ mol<sup>-1</sup>, respectively), whereas water desorption (step 3) features a high barrier ( $\Delta E_{des} = 177$  kJ mol<sup>-1</sup>). The latter step is the most difficult one in the O<sub>v</sub> formation pathway and limits the progress of the reaction. As water desorption is facilitated by a higher temperature, it leads to an increase in the number of oxygen vacancies and CO<sub>2</sub> adsorption. Consequently, the



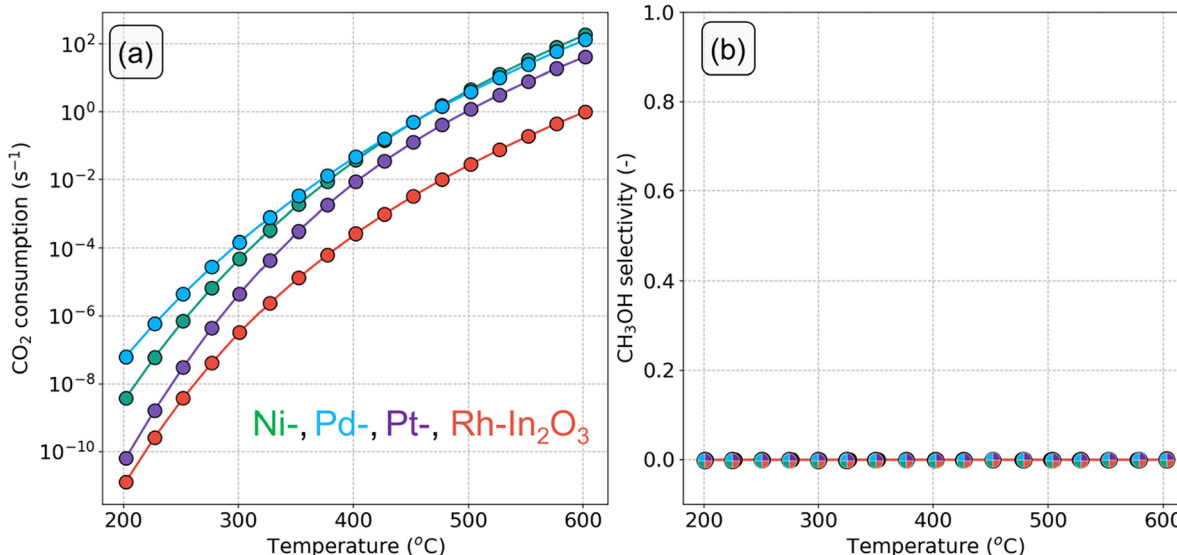


Fig. 5 (a) CO<sub>2</sub> consumption rate (s<sup>-1</sup>) and (b) CH<sub>3</sub>OH selectivity as a function of temperature on SA-In<sub>2</sub>O<sub>3</sub> models ( $p = 50$  bar, H<sub>2</sub>/CO<sub>2</sub> ratio = 5).

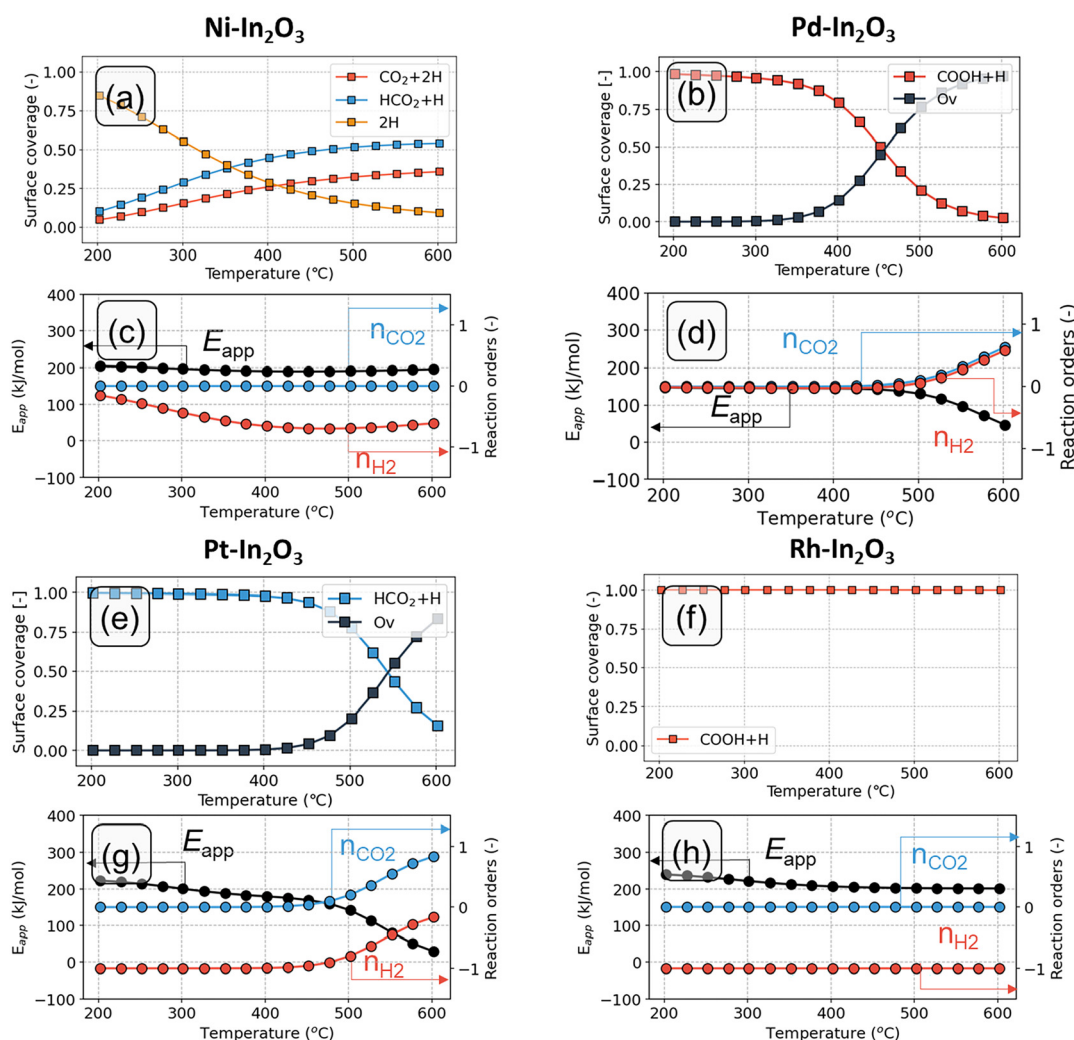


Fig. 6 Surface state of the catalyst as a function of temperature for (a) Ni-, (b) Pd- (e) Pt- and (f) Rh-In<sub>2</sub>O<sub>3</sub>, respectively. Apparent activation energy (in kJ mol<sup>-1</sup>) and reaction orders in CO<sub>2</sub> and H<sub>2</sub> as a function of temperature on (c) Ni-, (d) Pd- (g) Pt- and (h) Rh-In<sub>2</sub>O<sub>3</sub>, respectively.

coverage of the 2H state decreases and the coverage of intermediate states in the formate pathway to methanol ( $\text{CO}_2 + 2\text{H}$  and  $\text{HCO}_2 + \text{H}$ ) increases. At  $T > 400$  °C, the latter states become dominant. On the Ni-In<sub>2</sub>O<sub>3</sub> model, hydrogenation of  $\text{CO}_2$  to  $\text{HCO}_2$  (step 6) has an activation energy of 66 kJ mol<sup>-1</sup> and a reaction energy of -2 kJ mol<sup>-1</sup>. In contrast, subsequent hydrogenation to  $\text{H}_2\text{CO}_2$  (step 7) has a considerably higher activation energy of 114 kJ mol<sup>-1</sup> and is endothermic. As formation of  $\text{H}_2\text{CO}_2$  is difficult and the previous two states are comparable in terms of energy,  $\text{CO}_2 + 2\text{H}$  and  $\text{HCO}_2 + \text{H}$  are the dominant states. At low temperature, the model predicts a reaction order of nearly zero in  $\text{CO}_2$  and  $\text{H}_2$  (Fig. 6c). Under these conditions, the reaction is limited by the rate of  $\text{H}_2\text{O}$  removal, and an increase of the partial pressure of  $\text{CO}_2$  or  $\text{H}_2$  does not affect this process. Thus, the corresponding reaction orders in  $\text{CO}_2$  and  $\text{H}_2$  must be zero. At higher temperature, however, a negative reaction order in  $\text{H}_2$  is found. A higher partial pressure of  $\text{H}_2$  would lead to higher rates of H adsorption facilitating hydrogenation reactions. In turn, this pushes the reaction away from the CO product leading to a decrease in the overall rate. On the Ni-In<sub>2</sub>O<sub>3</sub> model, the apparent activation energy ( $E_{\text{app}}$ , Fig. 6c) has a constant value of at 175 kJ mol<sup>-1</sup> between 200 °C and 400 °C. This value corresponds to the desorption energy of  $\text{H}_2\text{O}$ . At higher temperature, a slight decrease in the  $E_{\text{app}}$  is observed, indicating a change in the rate-limiting step. This aspect will be clarified with a DRC analysis (*vide infra*).

On the Pd-In<sub>2</sub>O<sub>3</sub> model, the  $\text{COOH} + \text{H}$  is the dominant state at  $T < 450$  °C (Fig. 6b). Fig. 3b shows that hydrogenation of  $\text{CO}_2$  to  $\text{COOH}$  (step 16) and its subsequent dissociation into CO and OH are facile ( $E_{\text{act}} = 61$  kJ mol<sup>-1</sup> and  $E_{\text{act}} = 42$  kJ mol<sup>-1</sup>, respectively). However, the subsequent step of OH hydrogenation has a higher activation energy and is endothermic ( $E_{\text{act}} = 140$  kJ mol<sup>-1</sup> and  $E_{\text{R}} = 58$  kJ mol<sup>-1</sup>, respectively). This makes the conversion of the  $\text{COOH} + \text{H}$  state difficult. At high temperature ( $T > 450$  °C), the barrier for OH hydrogenation (step 17) can be more easily overcome, resulting in formation of oxygen vacancies. As a result, the dominant state becomes the Pd-In<sub>2</sub>O<sub>3</sub> surface with an oxygen vacancy (Ov). The model predicts a reaction order of zero in  $\text{CO}_2$  and  $\text{H}_2$  for  $T < 450$  °C (Fig. 6d). As the dominant working state already corresponds to intermediates derived from  $\text{H}_2$  and  $\text{CO}_2$ , a change in the partial pressure of these reactants does not impact the activity. For  $T > 450$  °C, the reaction orders in  $\text{CO}_2$  and  $\text{H}_2$  are positive, indicating that hydrogenation reactions are controlling the reaction rate. The  $E_{\text{app}}$  is approximately 150 kJ mol<sup>-1</sup> at 200 °C and decreases with increasing temperature (Fig. 6d).

On the Pt-In<sub>2</sub>O<sub>3</sub> model, the  $\text{HCO}_2 + \text{H}$  state is the dominant state for below 525 °C (Fig. 6e). Hydrogenation of  $\text{CO}_2$  to  $\text{HCO}_2$  (step 6 in Fig. 3c) is facile ( $E_{\text{act}} = 34$  kJ mol<sup>-1</sup>), while the subsequent step of  $\text{HCO}_2$  hydrogenation to  $\text{H}_2\text{CO}_2$  (step 7) is more difficult ( $E_{\text{act}} = 146$  kJ mol<sup>-1</sup>,  $E_{\text{R}} = +129$  kJ mol<sup>-1</sup>). This hampers the conversion of the  $\text{HCO}_2 + \text{H}$  state. At higher temperature, the surface coverage of the  $\text{HCO}_2 + \text{H}$

state decreases in favor of oxygen vacancies (Ov). The Ov state becomes dominant for  $T > 525$  °C. The reaction order in  $\text{CO}_2$  is zero at low temperature, because the surface is already covered with  $\text{HCO}_2 + \text{H}$  resulting from  $\text{CO}_2$  hydrogenation (Fig. 6g). At higher temperature ( $T > 475$  °C), the reaction order in  $\text{CO}_2$  becomes positive indicating that  $\text{CO}_2$  activation reactions are controlling the rate. The reaction order in  $\text{H}_2$  is negative, as also found for Ni- and Pd-In<sub>2</sub>O<sub>3</sub>. The  $E_{\text{app}}$  stays almost constant for temperature below 300 °C at 200 kJ mol<sup>-1</sup> and decreases with increasing temperature (Fig. 6g).

Within the temperature range of 200 °C and 600 °C, the dominant state of Rh-In<sub>2</sub>O<sub>3</sub> is the  $\text{COOH} + \text{H}$  state (Fig. 6f). The reason becomes apparent from inspection of Fig. 3d. Hydrogenation of  $\text{CO}_2$  to  $\text{COOH}$  and its further dissociation (step 16–17) are facile ( $E_{\text{act}} = 59$  and  $E_{\text{act}} = 25$  kJ mol<sup>-1</sup>, respectively). However, the subsequent step of OH hydrogenation is more difficult ( $E_{\text{act}} = 186$  kJ mol<sup>-1</sup>) and hampers the conversion of the  $\text{CO} + \text{OH}$  state. With respect to the dominant  $\text{COOH} + \text{H}$  state, an overall barrier of 341 kJ mol<sup>-1</sup> must be overcome to complete the H-assisted rWGS cycle (Fig. 4d). As a result, only for temperatures far above 600 °C, states other than  $\text{COOH} + \text{H}$  observed. The reaction order in  $\text{CO}_2$  is zero at low temperature, because the surface is already covered with  $\text{COOH} + \text{H}$  resulting from  $\text{CO}_2$  hydrogenation (Fig. 6h). The reaction order in  $\text{H}_2$  is negative, indicating that a higher partial pressure of  $\text{H}_2$  would push the reaction away from the dominant CO formation pathway. The apparent activation energy decreases from 260 kJ mol<sup>-1</sup> to 220 kJ mol<sup>-1</sup> between 200 and 400 °C (Fig. 6h).

### Sensitivity analysis

In this section, we analyse in more depth the steps that lead to  $\text{CH}_3\text{OH}$  and CO during  $\text{CO}_2$  hydrogenation on the SA-promoted In<sub>2</sub>O<sub>3</sub> models. We identify the elementary steps that control the overall  $\text{CO}_2$  consumption rate and the  $\text{CH}_3\text{OH}$  selectivity and investigate how these steps change with reaction temperature. For this purpose, we conduct a sensitivity analysis based on the degree of rate control (DRC) analysis.<sup>54</sup> At zero  $\text{CO}_2$  conversion, the sum of the DRC coefficients is conserved at unity.<sup>55</sup>

The DRC analysis and reaction flux analysis for the Ni-In<sub>2</sub>O<sub>3</sub> model are shown in Fig. 7a and b, respectively. At low temperature, the  $\text{CO}_2$  consumption rate is mostly controlled by water desorption (step 3) preceding oxygen vacancy formation (Fig. 7a). This result is in line with the dominant surface state being the 2H state, which precedes  $\text{H}_2\text{O}$  formation (Fig. 6a). Furthermore,  $\text{H}_2\text{O}$  desorption has the highest barrier in the oxygen vacancy formation pathway ( $\Delta E_{\text{des}} = 177$  kJ mol<sup>-1</sup>), making formation of an oxygen vacancy difficult. At higher temperature ( $T > 275$  °C), water desorption results in oxygen vacancies and  $\text{CO}_2$  adsorption. As a result, the DRC coefficient of the  $\text{H}_2\text{O}$  desorption step decreases, in favor of the  $\text{CO}_2$  dissociation step (step 12). At higher temperature, the latter becomes the main rate-limiting step. An increased rate of  $\text{CO}_2$  dissociation would



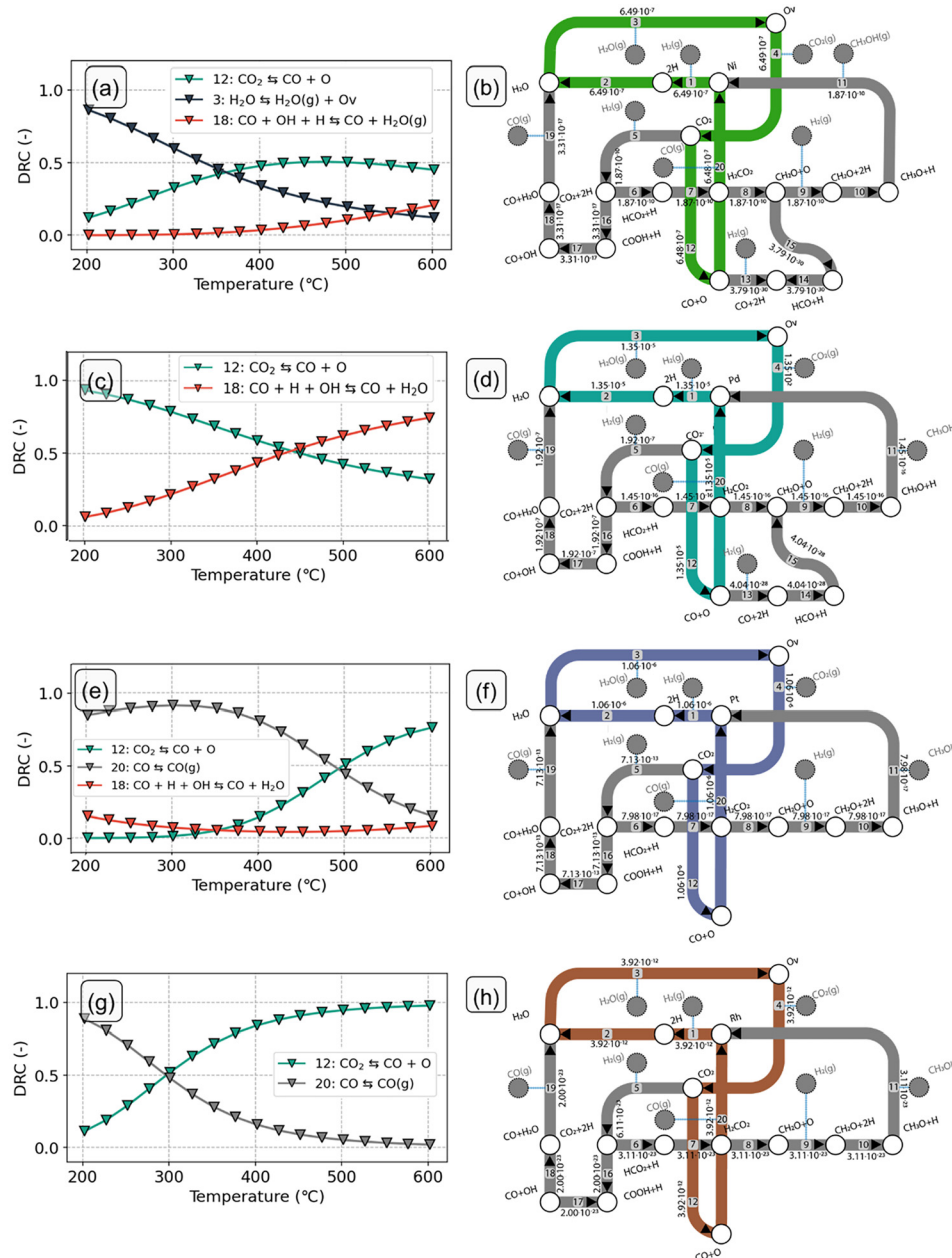


**Fig. 7** Degree of rate control and molar fluxes analysis for (a and b) Ni-, (c and d) Pd, (e and f) Pt and (g and h) Rh-In<sub>2</sub>O<sub>3</sub> models. The numbers in the arrows are molar reaction rates ( $\text{s}^{-1}$ ) and are normalized with respect to the amount of adsorbed  $\text{CO}_2$ . The dominant pathway for each model is indicated by the colored pathways. The molar fluxes are reported at  $T = 200$  °C.

result in a higher flux towards CO, benefiting the formation of this product. The dominant pathway (Fig. 7b) on the Ni-In<sub>2</sub>O<sub>3</sub> model proceeds *via* formation of an oxygen vacancy followed by  $\text{CO}_2$  adsorption and direct dissociation. The carboxyl pathway to CO is not taken because OH removal (step 18) is associated with a higher barrier than direct  $\text{CO}_2$  dissociation ( $E_{\text{act}} = 140$  kJ mol<sup>-1</sup> and  $E_{\text{act}} = 81$  kJ mol<sup>-1</sup>, respectively). Compared to the dominant pathway to CO, methanol formation pathways feature considerably lower molar fluxes. This is in keeping with our finding that Ni-In<sub>2</sub>O<sub>3</sub> mainly produces CO. The formate pathway is not taken because the steps of  $\text{H}_2\text{CO}$  hydrogenation to  $\text{H}_2\text{CO}_2$  and its

further dissociation into  $\text{CH}_2\text{O}$  and O (steps 7–8) result in a combined reaction energy of +180 kJ mol<sup>-1</sup>. Hydrogenation of CO to methanol does not proceed because  $\text{CH}_2\text{O}$  formation from HCO has a high activation energy and is endothermic ( $E_{\text{act}} = 177$  kJ mol<sup>-1</sup> and  $E_r = 142$  kJ mol<sup>-1</sup>, respectively).

For Pd-In<sub>2</sub>O<sub>3</sub> (Fig. 7c), for  $T < 425$  °C, the overall rate is mostly controlled by  $\text{CO}_2$  dissociation (step 12,  $E_{\text{act}} = 65$  kJ mol<sup>-1</sup>). The dominant pathway on the Pd-In<sub>2</sub>O<sub>3</sub> surface proceeds *via* formation of an oxygen vacancy and direct dissociation of  $\text{CO}_2$  (Fig. 7d). At higher temperature ( $T > 400$  °C), a decrease in the DRC coefficient of step 12 is observed in favor of the step of OH removal in the carboxyl pathway

(step 18,  $E_{act} = 140 \text{ kJ mol}^{-1}$ ) which becomes the main rate limiting step. The change in rate limiting steps indicates a change in the dominant pathway. Indeed, for  $T > 425 \text{ }^\circ\text{C}$ , the carboxyl pathway is the dominant pathway of CO formation (Fig. S7†). Furthermore, this is in line with the increasing reaction order in  $\text{H}_2$  with increasing temperature (Fig. 6d). Compared to the dominant pathway to CO, methanol formation pathways have considerably lower molar fluxes. The formate pathway is not taken because the step of  $\text{HCO}_2$  hydrogenation to  $\text{H}_2\text{CO}_2$  has a high activation energy ( $E_{act} = 220 \text{ kJ mol}^{-1}$ ) and is endothermic ( $E_r = 167 \text{ kJ mol}^{-1}$ ). Furthermore, hydrogenation of CO to  $\text{CH}_3\text{OH}$  does not take place because the hydrogenation of CO to HCO has an activation energy of  $148 \text{ kJ mol}^{-1}$ , significantly higher than the CO desorption energy ( $31 \text{ kJ mol}^{-1}$ ). This makes further CO hydrogenation less favorable than its desorption.

The DRC analysis and reaction flux analysis for the Pt- $\text{In}_2\text{O}_3$  model are shown in Fig. 7e and f, respectively. At low temperature, the overall rate of is mainly controlled by CO desorption (step 20,  $\Delta E_{des} = 158 \text{ kJ mol}^{-1}$ ). OH hydrogenation (step 18,  $E_{act} = 133 \text{ kJ mol}^{-1}$ ) controls the rate to a smaller extent as can be seen by its lower DRC coefficient. In line with Ni- $\text{In}_2\text{O}_3$ , the dominant pathway proceeds *via* formation of an oxygen vacancy and direct dissociation of  $\text{CO}_2$  (Fig. 7f). The carboxyl pathway is not taken because COOH formation and OH removal are associated with high barriers ( $E_{act} = 147 \text{ kJ mol}^{-1}$  and  $E_{act} = 133 \text{ kJ mol}^{-1}$ , respectively). With increasing temperature, the DRC coefficient of CO desorption decreases in favor of  $\text{CO}_2$  dissociation (step 12). This is in line with the positive reaction order in  $\text{CO}_2$  calculated at higher temperature (Fig. 6e). Compared to the dominant pathway to CO, hydrogenation of  $\text{CO}_2$  to methanol is associated with significantly lower molar fluxes. The formate pathway is not taken because the hydrogenation of  $\text{HCO}_2$  to  $\text{H}_2\text{CO}_2$  has a high activation energy and is endothermic ( $E_{act} = 146 \text{ kJ mol}^{-1}$ ,  $E_r = 129 \text{ kJ mol}^{-1}$ ).

On Rh- $\text{In}_2\text{O}_3$ , for  $T < 300 \text{ }^\circ\text{C}$ , the rate of  $\text{CO}_2$  consumption is mainly controlled by CO desorption (step 20,  $\Delta E_{des} = 215 \text{ kJ mol}^{-1}$ ). At higher temperature, the DRC coefficient of this elementary step decreases in favour of  $\text{CO}_2$  dissociation (step 12,  $E_{act} = 81 \text{ kJ mol}^{-1}$ ) that becomes the rate determining step (RDS) at  $T > 450 \text{ }^\circ\text{C}$ . In line with the other SA- $\text{In}_2\text{O}_3$  models, the dominant pathway proceeds *via* formation of an oxygen vacancy and direct dissociation of  $\text{CO}_2$  (Fig. 7h). The high barrier associated with OH hydrogenation (step 18,  $E_{act} = 186 \text{ kJ mol}^{-1}$ ) hampers the carboxyl pathway. Compared to the dominant pathway to CO, methanol synthesis from  $\text{CO}_2$  is associated with significantly lower molar fluxes. The formate pathway is not taken because the hydrogenation of  $\text{HCO}_2$  to  $\text{H}_2\text{CO}_2$  has a high activation energy and is endothermic ( $E_{act} = 155 \text{ kJ mol}^{-1}$ ,  $E_r = 136 \text{ kJ mol}^{-1}$ ).

## General discussion

The present study clarifies the role of single atoms of Pt, Pd, Ni and Rh adsorbed on the  $\text{In}_2\text{O}_3(111)$  surface in  $\text{CO}_2$

hydrogenation. The explored reaction mechanism includes a direct route for  $\text{CO}_2$  hydrogenation to methanol (formate pathway), a pathway to methanol *via* CO hydrogenation and the competing reverse water-gas shift (rWGS) reaction. Earlier studies pointed out that SAs on the  $\text{In}_2\text{O}_3$  surface do not catalyse  $\text{CH}_4$  formation.<sup>29,30,35</sup> A key result of this study is that CO is the dominant reaction product for all SA- $\text{In}_2\text{O}_3$  models. CO is obtained *via* a redox mechanism involving oxygen vacancy formation followed by  $\text{CO}_2$  adsorption and direct C–O bond cleavage. On all models, the  $\text{CH}_3\text{OH}$  selectivity was found to be negligibly small, because barriers associated with the hydrogenation of formate intermediates to methanol are significantly higher than those for the dominant redox pathway to CO.

Methanol formation on  $\text{In}_2\text{O}_3$  involves the formation of oxygen vacancies and hydrogenation of formate intermediates.<sup>63,66</sup> On the unpromoted  $\text{In}_2\text{O}_3(111)$  surface, oxygen vacancy formation has an overall barrier of  $67 \text{ kJ mol}^{-1}$  with respect to gas-phase  $\text{H}_2$ .<sup>59,63</sup> When a single Pd, Pt or Rh atom is adsorbed on  $\text{In}_2\text{O}_3$ , oxygen vacancy formation exhibits comparable overall barriers of respectively  $62$ ,  $48$  and  $57 \text{ kJ mol}^{-1}$ . In contrast, a much higher overall barrier of  $150 \text{ kJ mol}^{-1}$  is computed for the single Ni atom on  $\text{In}_2\text{O}_3(111)$ . Concerning the conversion of formate,  $\text{HCO}_2$  hydrogenation to  $\text{H}_2\text{CO}_2$  on an  $\text{In}_2\text{O}_3(110)$  surface was earlier found to exhibit an activation energy of  $55 \text{ kJ mol}^{-1}$  and a reaction energy of  $+5 \text{ kJ mol}^{-1}$ .<sup>60</sup> On  $\text{In}_2\text{O}_3(111)$ , similar activation and reaction energies are found ( $98$  and  $15 \text{ kJ mol}^{-1}$ , respectively).<sup>57</sup> All SA- $\text{In}_2\text{O}_3$  models show higher activation energies for this step (step 7 in Fig. 3), which is the main cause of the very low methanol formation rate. We performed a sensitivity analysis of the microkinetic simulations involving decreasing the activation energies of steps 7 by  $10$ ,  $20$ ,  $30$  and  $40 \text{ kJ mol}^{-1}$ . The results given in Fig. S8† show that decreasing barriers result in a higher methanol selectivity for Ni-, Pt- and Rh- $\text{In}_2\text{O}_3$ . Herein, we consider methanol selectivity of at least  $1\%$  as significant. Methanol formation is least improved for Pd- $\text{In}_2\text{O}_3$ , because the activation energy associated with  $\text{HCO}_2$  hydrogenation (step 7) is very high ( $220 \text{ kJ mol}^{-1}$ ). In this case, a decrease of at least  $80 \text{ kJ mol}^{-1}$  is required to obtain significant  $\text{CH}_3\text{OH}$  selectivity. We extended the sensitivity analysis to include  $\text{H}_2\text{CO}_2$  dissociation (step 8) and reported the results in Fig. S9.† Also in this case, decreasing barriers results in a higher methanol selectivity for Ni-, Pt- and Rh- $\text{In}_2\text{O}_3$ , whereas methanol formation is less improved for Pd- $\text{In}_2\text{O}_3$  because the previous step has a higher barrier ( $220 \text{ kJ mol}^{-1}$  and  $62 \text{ kJ mol}^{-1}$  for steps 7–8, respectively).

Our microkinetic simulations show that all SA- $\text{In}_2\text{O}_3$  have CO as the main product obtained *via* a redox mechanism. The activity for the rWGS reaction decreases in the order Pd  $>$  Ni  $>$  bare  $\text{In}_2\text{O}_3$   $>$  Pt  $>$  Rh (Fig. S6d†). We now explain this finding based on the DFT-computed activation energies and the analysis of the rate limiting steps. On all SA- $\text{In}_2\text{O}_3$  models, direct  $\text{CO}_2$  dissociation (step 12) and subsequent CO desorption (step 20) are the main rate-limiting steps towards



CO formation. On Pd-In<sub>2</sub>O<sub>3</sub>, these steps have barriers of 65 and 31 kJ mol<sup>-1</sup>, respectively. On Ni-In<sub>2</sub>O<sub>3</sub>, direct CO<sub>2</sub> dissociation and CO desorption are associated with barriers of 91 and 80 kJ mol<sup>-1</sup>, respectively. On bare-In<sub>2</sub>O<sub>3</sub>, CO is obtained *via* carboxyl pathway involving a COOH intermediate. This pathway is mainly limited by the rate of COOH dissociation which is associated with a high barrier ( $E_{act} = 150$  kJ mol<sup>-1</sup>). Compared to Ni and Pd-In<sub>2</sub>O<sub>3</sub>, the barrier for CO<sub>2</sub> dissociation on Pt-In<sub>2</sub>O<sub>3</sub> is similar ( $E_{act} = 65$  kJ mol<sup>-1</sup>), but CO desorption is associated with a higher barrier ( $\Delta E_{des} = 158$  kJ mol<sup>-1</sup>). On Rh-In<sub>2</sub>O<sub>3</sub>, desorption of CO is associated with a high desorption energy ( $\Delta E_{des} = 215$  kJ mol<sup>-1</sup>) hampering its formation. For this reason, this model shows the lowest activity to CO.

We know explain why the redox pathway is preferred over the carboxyl pathway for the formation of CO on our SA-In<sub>2</sub>O<sub>3</sub> models. In the redox pathway, the C–O bond in CO<sub>2</sub> is broken directly resulting in CO binding to the SA and the O healing the vacancy. This process is associated with relatively low barriers on all models, in line with the strong SA–O bond (Table S14†). Notably, on a bare In<sub>2</sub>O<sub>3</sub>(110) surface, where CH<sub>3</sub>OH is the main product, replenishing the oxygen vacancy by CO<sub>2</sub> dissociation is associated with a reaction energy of 1.4 eV.<sup>60</sup> This indicates that direct CO<sub>2</sub> dissociation would have a barrier of at least 1.4 eV, making this elementary reaction step unlikely. In contrast with SA-promoted In<sub>2</sub>O<sub>3</sub>, on bare-In<sub>2</sub>O<sub>3</sub>, there is no active site available for accepting the CO molecule resulting from CO<sub>2</sub> dissociation. On the SA-In<sub>2</sub>O<sub>3</sub> models, breaking the C–O bond on a COOH intermediate is also possible, however the subsequent step of OH removal *via* H<sub>2</sub>O formation is associated with high barriers because it requires the migration of a OH moiety to the SA.

A fundamental assumption in this study was that each kinetic pathway features one oxygen vacancy, in line with previous DFT calculations on In<sub>2</sub>O<sub>3</sub>.<sup>19,21,22</sup> To investigate whether the presence of a second oxygen vacancy could change the conclusions of this work, we calculated a few key elementary steps relevant to such a mechanism. The results are reported in Tables S15–S18† reveal that a second vacancy provides a lower activation energy for some elementary reaction steps. However, these deviations are not significant enough to impact the dominant pathway identified in our microkinetic simulations. Consequently, we deduce that the inclusion of a second oxygen vacancy does not change the conclusions put forth in this study.

We also compare our results to those recently reported in the literature. In line with the present work, Frei *et al.* concluded from DFT calculations that a Ni SA on In<sub>2</sub>O<sub>3</sub> would be active for the rWGS, because it features lower barriers compared to CO<sub>2</sub> hydrogenation to methanol.<sup>29</sup> Furthermore, Millet *et al.* showed that isolated Ni atoms in a Ni<sub>1-x</sub>Mg<sub>x</sub>O catalyst are active for the rWGS but are unable to catalyse CO<sub>2</sub> hydrogenation to CH<sub>4</sub> (or MeOH), for which Ni clusters are needed.<sup>67</sup> Indeed, Shen *et al.* deployed DFT to compare various pathways of CO<sub>2</sub> hydrogenation to methanol

on a Ni<sub>4</sub>/In<sub>2</sub>O<sub>3</sub>(111) model and found that methanol can be obtained *via* CO intermediate obtained by rWGS.<sup>68</sup> In an earlier computational work, we reported that single atoms of Ni either doped in or adsorbed on In<sub>2</sub>O<sub>3</sub>(111) surface would mainly catalyze CO formation, whereas small Ni clusters would mainly lead to methanol.<sup>27</sup> In line with this earlier work, we indicate here that the Ni-In<sub>2</sub>O<sub>3</sub> model features low-barrier CO<sub>2</sub> dissociation resulting in a preference for CO formation over hydrogenation to methanol. Ye *et al.* reported that methanol is the main product of CO<sub>2</sub> hydrogenation *via* formate on a Pd<sub>4</sub>/In<sub>2</sub>O<sub>3</sub>(111) model.<sup>62</sup> Our Pd-In<sub>2</sub>O<sub>3</sub> model features higher barriers for the formate pathway compared to direct CO<sub>2</sub> dissociation precluding methanol formation in favor of CO. Liu *et al.* reported that methanol formation on a Pt<sub>4</sub>/In<sub>2</sub>O<sub>3</sub>(111) model takes place *via* hydrogenation of CO resulting from CO<sub>2</sub> dissociation.<sup>32</sup> Our Pt-In<sub>2</sub>O<sub>3</sub> model does not allow a TS for the subsequent hydrogenation steps of CO to HCO and H<sub>2</sub>CO precluding methanol formation from CO hydrogenation. Clusters of Pd, Pt or Ni on the In<sub>2</sub>O<sub>3</sub>(111) surface catalyze the formation of methanol because hydrogenation of either formate or CO is favored over the rWGS reaction to CO. However, in the limit of a single atom of Pd, Pt or Ni on the In<sub>2</sub>O<sub>3</sub>(111) surface, pathways leading to methanol have higher barriers than the redox pathway to CO resulting in low methanol selectivity. In a recent theoretical study, Pinheiro Araújo *et al.* studied atomically dispersed metal atoms (Pd, Pt, Rh, Ni, Co, Au, Ir) on the In<sub>2</sub>O<sub>3</sub> surface.<sup>28</sup> They speculated on the basis of energy diagrams that CO<sub>2</sub> hydrogenation to methanol *via* formate is favored over CO formation. Although this conclusion is at odds with our finding from microkinetic simulations that CO<sub>2</sub> hydrogenation on SA-promoted In<sub>2</sub>O<sub>3</sub> would mainly lead to CO, it can be understood from the fact that the study of Pinheiro Araújo *et al.* only considered the COOH pathway to CO, *i.e.*, they omitted the redox pathway.

## Conclusions

Using microkinetic models and DFT calculations, we clarified the role of single atoms (SA) on In<sub>2</sub>O<sub>3</sub> in CO<sub>2</sub> hydrogenation to CH<sub>3</sub>OH and CO. We investigated the role of single atoms of Pt, Pd, Ni and Rh on the (111) surface of In<sub>2</sub>O<sub>3</sub> for the formation of methanol *via* formate and CO as well as the competing rWGS reaction *via* redox and carboxyl pathways. Compared to the pristine In<sub>2</sub>O<sub>3</sub>(111) surface, adsorbing a single Pd, Pt or Rh atom results in comparable overall barriers for oxygen vacancy formation. In contrast, the presence of a single Ni atom on the In<sub>2</sub>O<sub>3</sub> surface increases the overall barrier for oxygen vacancy formation significantly. Microkinetic simulations reveal that all SA-In<sub>2</sub>O<sub>3</sub> models mainly catalyze CO *via* formation of an oxygen vacancy followed by CO<sub>2</sub> adsorption and direct C–O bond cleavage (redox pathway). The carboxyl pathway to CO is not taken, because OH removal resulting from COOH dissociation is associated with higher barriers compared to the dominant redox pathway. The model predicts that Pd is the preferred



promoter for  $\text{In}_2\text{O}_3$  model, achieving the highest activity among the transition metals considered due to a low barrier for  $\text{CO}_2$  dissociation and a relatively weak adsorption strength of the CO product. For all models, the  $\text{CH}_3\text{OH}$  selectivity is negligibly low because high barriers are associated with the hydrogenation of  $\text{HCO}_2$  to  $\text{H}_2\text{CO}_2$  and its subsequent dissociation into  $\text{CH}_2\text{O}$  (formate pathway) compared to the dominant rWGS pathway.

## Author contributions

Francesco Cannizzaro: DFT calculations, microkinetic modelling, writing and visualization. Sjoerd Kurstjens and Tom van den Berg: DFT calculations. Emiel J.M. Hensen and Ivo Pilot resources, conceptualization, supervision.

## Conflicts of interest

There are no conflicts to declare.

## Acknowledgements

The authors acknowledge NWO and SurfSARA for providing access to computational resources used to carry out the DFT calculations reported in this work. This work was supported by the Netherlands Center for Multiscale Catalytic Energy Conversion (MCEC), an NWO Gravitation program funded by the Ministry of Education, Culture and Science of the government of the Netherlands. This project has received funding from the European Union's Horizon 2020 research and innovation program under the Marie Skłodowska-Curie grant agreement No 801359.

## Notes and references

- 1 A. González-Garay, M. S. Frei, A. Al-Qahtani, C. Mondelli, G. Guillén-Gosálbez and J. Pérez-Ramírez, *Energy Environ. Sci.*, 2019, **12**, 3425–3436.
- 2 E. V. Kondratenko, G. Mul, J. Baltrusaitis, G. O. Larrazábal and J. Pérez-Ramírez, *Energy Environ. Sci.*, 2013, **6**, 3112.
- 3 V. Dias, M. Pochet, F. Contino and H. Jeanmart, *Front. Mech. Eng.*, 2020, **6**, 21.
- 4 A. Álvarez, A. Bansode, A. Urakawa, A. V. Bavykina, T. A. Wezendonk, M. Makkee, J. Gascon and F. Kapteijn, *Chem. Rev.*, 2017, **117**, 9804–9838.
- 5 J. Zhong, X. Yang, Z. Wu, B. Liang, Y. Huang and T. Zhang, *Chem. Soc. Rev.*, 2020, **49**, 1385–1413.
- 6 X. Jiang, X. Nie, X. Guo, C. Song and J. G. Chen, *Chem. Rev.*, 2020, **120**, 7984–8034.
- 7 J. Wang, G. Zhang, J. Zhu, X. Zhang, F. Ding, A. Zhang, X. Guo and C. Song, *ACS Catal.*, 2021, **2020**, 1406–1423.
- 8 Y. A. Daza and J. N. Kuhn, *RSC Adv.*, 2016, **6**, 49675–49691.
- 9 S. Saeidi, N. A. S. Amin and M. R. Rahimpour, *J. CO<sub>2</sub> Util.*, 2014, **5**, 66–81.
- 10 W. Li, H. Wang, X. Jiang, J. Zhu, Z. Liu, X. Guo and C. Song, *RSC Adv.*, 2018, **8**, 7651–7669.

- 11 S. Gumber and A. V. P. Gurumoorthy, *Methanol Sci. Eng.*, 2018, pp. 661–674.
- 12 G. A. Olah, *Angew. Chem., Int. Ed.*, 2005, **44**, 2636–2639.
- 13 A. Goeppert, M. Czaun, J. P. Jones, G. K. Surya Prakash and G. A. Olah, *Chem. Soc. Rev.*, 2014, **43**, 7995–8048.
- 14 C. Baltes, S. Vukojević and F. Schüth, *J. Catal.*, 2008, **258**, 334–344.
- 15 M. Behrens, *Angew. Chem., Int. Ed.*, 2016, **55**, 14906–14908.
- 16 J. Nakamura, Y. Choi and T. Fujitani, *Top. Catal.*, 2003, **22**, 277–285.
- 17 M. B. Fichtl, D. Schlereth, N. Jacobsen, I. Kasatkin, J. Schumann, M. Behrens, R. Schlögl and O. Hinrichsen, *Appl. Catal., A*, 2015, **502**, 262–270.
- 18 X. Jiang, X. Nie, X. Guo, C. Song and J. G. Chen, *Chem. Rev.*, 2020, **120**, 7984–8034.
- 19 J. Ye, C. Liu and Q. Ge, *J. Phys. Chem. C*, 2012, **116**, 7817–7825.
- 20 M. S. Frei, C. Mondelli, A. Cesarini, F. Krumeich, R. Hauer, J. A. Stewart, D. Curulla Ferré and J. Pérez-Ramírez, *ACS Catal.*, 2020, **10**, 1133–1145.
- 21 Q. Sun, J. Ye, C. Liu and Q. Ge, *Greenhouse Gases: Sci. Technol.*, 2014, **4**, 140–144.
- 22 J. Ye, C. Liu, D. Mei and Q. Ge, *ACS Catal.*, 2013, **3**, 1296–1306.
- 23 A. Cao, Z. Wang, H. Li and J. K. Nørskov, *ACS Catal.*, 2021, **11**, 1780–1786.
- 24 J. Wang, G. Zhang, J. Zhu, X. Zhang, F. Ding, A. Zhang, X. Guo and C. Song, *ACS Catal.*, 2021, **11**, 1406–1423.
- 25 A. Posada-Borbón and H. Grönbeck, *ACS Catal.*, 2021, **11**, 9996–10006.
- 26 J. Zhu, F. Cannizzaro, L. Liu, H. Zhang, N. Kosinov, I. A. W. Pilot, J. Rabieah, A. Brückner and E. J. M. Hensen, *ACS Catal.*, 2021, **11**, 11371–11384.
- 27 F. Cannizzaro, E. J. M. Hensen and I. A. W. Pilot, *ACS Catal.*, 2023, **13**, 1875–1892.
- 28 T. Pinheiro Araújo, J. Morales-Vidal, T. Zou, R. García-Muelas, P. O. Willi, K. M. Engel, O. V. Safonova, D. Faust Akl, F. Krumeich, R. N. Grass, C. Mondelli, N. López and J. Pérez-Ramírez, *Adv. Energy Mater.*, 2022, **12**, 14.
- 29 M. S. Frei, C. Mondelli, R. García-Muelas, J. Morales-Vidal, M. Philipp, O. V. Safonova, N. López, J. A. Stewart, D. C. Ferré and J. Pérez-Ramírez, *Nat. Commun.*, 2021, **12**, 2–12.
- 30 M. S. Frei, C. Mondelli, R. García-Muelas, K. S. Kley, B. Puértolas, N. López, O. V. Safonova, J. A. Stewart, D. Curulla Ferré and J. Pérez-Ramírez, *Nat. Commun.*, 2019, **10**, 1–11.
- 31 Z. Han, C. Tang, J. Wang, L. Li and C. Li, *J. Catal.*, 2021, **394**, 236–244.
- 32 K. Sun, N. Rui, C. Shen and C. J. Liu, *J. Phys. Chem. C*, 2021, **125**, 10926–10936.
- 33 J. Wang, K. Sun, X. Jia and C. J. Liu, *Catal. Today*, 2021, **365**, 341–347.
- 34 N. H. M. Dostagir, C. Thompson, H. Kobayashi, A. M. Karim, A. Fukuoka and A. Shrotri, *Catal. Sci. Technol.*, 2020, **10**, 8196–8202.



35 N. H. M. Dostagir, C. Thompson, H. Kobayashi, A. M. Karim, A. Fukuoka and A. Shrotri, *Catal. Sci. Technol.*, 2020, **10**, 8196–8202.

36 X. Jia, K. Sun, J. Wang, C. Shen and C. J. Liu, *J. Energy Chem.*, 2020, **50**, 409–415.

37 J. Ye, C. J. Liu, D. Mei and Q. Ge, *J. Catal.*, 2014, **317**, 453.

38 G. Kresse and D. Joubert, *Phys. Rev. B: Condens. Matter Mater. Phys.*, 1999, **59**, 1758.

39 J. P. Perdew, K. Burke and M. Ernzerhof, *Phys. Rev. Lett.*, 1996, **77**, 3865.

40 G. Kresse and J. Hafner, *Phys. Rev. B: Condens. Matter Mater. Phys.*, 1994, **49**, 14251–14269.

41 G. Kresse and J. Furthmüller, *Comput. Mater. Sci.*, 1996, **6**, 15–50.

42 G. Henkelman and H. Jónsson, *J. Chem. Phys.*, 2000, **113**, 9978–9985.

43 D. Heidrich and W. Quapp, *Theor. Chim. Acta*, 1986, **70**, 89–98.

44 R. Nelson, C. Ertural, J. George, V. L. Deringer, G. Hautier and R. Dronskowski, *J. Comput. Chem.*, 2020, **41**, 1931–1940.

45 S. Maintz, V. L. Deringer, A. L. Tchougr and R. Dronskowski, *J. Comput. Chem.*, 2016, **37**, 11–12.

46 M. Yu and D. R. Trinkle, *J. Chem. Phys.*, 2011, **134**, 064111.

47 P. N. Brown, G. D. Byrne and A. C. Hindmarsh, *SIAM Journal on Scientific and Statistical Computing*, 2006, **10**, 1038–1051.

48 G. D. Byrne and A. C. Hindmarsh, *J. Comput. Phys.*, 1987, **70**, 1–62.

49 G. D. Byrne and A. C. Hindmarsh, *ACM Trans. Math. Softw.*, 1975, **1**, 71–96.

50 C. H. Shomate, *J. Phys. Chem.*, 2002, **58**, 368–372.

51 NIST Chemistry WebBook, <https://webbook.nist.gov/chemistry/>, (accessed 1 February 2022).

52 S. Kozuch and S. Shaik, *J. Am. Chem. Soc.*, 2006, **128**, 3355–3365.

53 S. Kozuch and S. Shaik, *J. Phys. Chem. A*, 2008, **112**, 6032–6041.

54 C. T. Campbell, *ACS Catal.*, 2017, **7**, 2770–2779.

55 A. W. Filot, *Introduction to Microkinetic Modeling*, Technische Universiteit Eindhoven, 2017.

56 C. Stegelmann, N. C. Schiødt, C. T. Campbell and P. Stoltze, *J. Catal.*, 2004, **221**, 630–649.

57 M. S. Frei, M. Capdevila-Cortada, R. García-Muelas, C. Mondelli, N. López, J. A. Stewart, D. Curulla Ferré and J. Pérez-Ramírez, *J. Catal.*, 2018, **361**, 313–321.

58 M. S. Frei, C. Mondelli, R. García-Muelas, J. Morales-Vidal, M. Philipp, O. V. Safonova, N. López, J. A. Stewart, D. C. Ferré and J. Pérez-Ramírez, *Nat. Commun.*, 2021, **12**, 1–9.

59 D. Albani, M. Capdevila-Cortada, G. Vilé, S. Mitchell, O. Martin, N. López and J. Pérez-Ramírez, *Angew. Chem., Int. Ed.*, 2017, **56**, 10755–10760.

60 J. Ye, C. Liu, D. Mei and Q. Ge, *ACS Catal.*, 2013, **3**, 1296–1306.

61 J. Ye, C. Liu and Q. Ge, *J. Phys. Chem. C*, 2012, **116**, 7817–7825.

62 J. Ye, C. J. Liu, D. Mei and Q. Ge, *J. Catal.*, 2014, **317**, 44–53.

63 M. S. Frei, M. Capdevila-Cortada, R. García-Muelas, C. Mondelli, N. López, J. A. Stewart, D. Curulla Ferré and J. Pérez-Ramírez, *J. Catal.*, 2018, **361**, 313–321.

64 X. Liu, L. Sun and W. Q. Deng, *J. Phys. Chem. C*, 2018, **122**, 8306–8314.

65 J. Ye, C. Liu, D. Mei and Q. Ge, *ACS Catal.*, 2013, **3**, 1296–1306.

66 J. Ye, C. Liu, D. Mei and Q. Ge, *ACS Catal.*, 2013, **3**, 1296–1306.

67 M. Millet, G. Algara-Siller, S. Wrabetz, A. Mazheika, F. Girgsdies, D. Teschner, F. Seitz, A. Tarasov, S. Levchenko, R. Schlögl and E. Frei, *J. Am. Chem. Soc.*, 2019, **6**, 2451–2461.

68 C. Shen, Q. Bao, W. Xue, K. Sun, Z. Zhang, X. Jia, D. Mei and C. J. Liu, *J. Energy Chem.*, 2022, **65**, 623–629.

